Check for updates

Preparation, characterization and application of polymeric ultra-permeable biodegradable ferromagnetic nanocomposite adsorbent for removal of Cr(VI) from synthetic wastewater: kinetics, isotherms and thermodynamics

Evans Suter[1]*, Hilary Rutto[1], Robert Makomere[1], Musamba Banza[1], Tumisang Seodigeng[1], Sammy Kiambi[1] and Wesley Omwoyo[2]

[1]Department of Chemical Engineering and Metallurgy, Clean Technology and Applied Materials Research Group, Vaal University of Technology, Vanderbijlpark, South Africa, [2]Biotechnology and Chemistry Department, Vaal University of Technology, Vanderbijlpark, South Africa

Hexavalent chromium (Cr(VI)) contamination in drinking water due to industrial activities is a growing worldwide concern. Cr(VI) concentrations exceeding a few parts per billion (ppb) can cause serious health problems such as asthma, blood cancer, kidney-related diseases, liver and spleen damage, as well as neurological system, immunological deficiencies, and reproductive issues. This study, thus, explored the feasibility of employing a novel polymeric ferromagnetic nanocomposite adsorbent made of low-cost, biodegradable, and ultra-permeable materials from pulp and paper sludge for adsorptive removal of hexavalent chromium (Cr^{6+}) from synthetic wastewater. Vibrating-sample magnetometer (VSM), X-ray diffraction (XRD), scanning electron microscopy (SEM), Brunauer-Emmet-Teller surface area (BET), and Fourier transform infrared (FTIR) were used to analyze the produced nanocomposite adsorbent. The Fourier transform infrared results confirmed the presence of adsorptive peaks attributed to $-OH$, $-NH2$, and FeO. Scanning electron microscopy micrographs revealed a porous adsorbent surface. XRD revealed the existence of the crystalline spinel-structured magnetite (Fe_3O_4) phase of iron oxide, while the saturation magnetization was established to be 26.90 emu/g. The Brunauer−Emmett−Teller analysis confirmed a slight decrease in the surface area of the nanocomposite adsorbent to 6.693 $m^2.g^{-1}$, compared to Fe_3O_4 (7.591 $m^2.g^{-1}$). The optimum conditions for Cr^{6+} removal were pH 2.0, 1.0 g/L adsorbent dose, room temperature (25°C), 120 min contact time, and 20 mg/L pollutant concentration. During removal, the Cr(VI) was adsorbed by electrostatic attraction and/or reduced to trivalent chromium Cr(III). At low starting Cr(VI) concentrations, chemisorption dominated the removal process, but as concentrations increased, physisorption became more significant. The

prepared nanocomposite adsorbent presented exceptional removal efficiency of up to 92.23%, indicating that it may be useful for the adsorption of metal ions from industrial and household wastewater.

1 Introduction

The existence of heavy metals, particularly in drinking water, has gained extensive public attention in recent years (Joseph et al., 2019). Water pollution from natural processes and anthropogenic activities has potentially harmful consequences due to rapid transportation, bioaccumulation, and biomagnification of organic and inorganic pollutants from abiotic to biotic environments (Hassan et al., 2021). Toxic trace metals are non-biodegradable and remain in the environment for decades (El-Kady and Abdel-Wahhab, 2018). Hexavalent chromium (Cr(VI)), in particular, is the 17th most hazardous substance in the environment (Wise Jr et al., 2022) and is classified as Group 1 by the International Agency for Research on Cancer (IARC) owing to its carcinogenicity to humans (Braver-Sewradj et al., 2021). Consumption of hexavalent chromium-polluted water may result in health-related effects, such as brain, liver, and central nervous system damage (Braver-Sewradj et al., 2021). To reduce Cr(VI) discharge into the environment, the United States Environmental Protection Agency (US EPA) limits drinking water and groundwater to 0.05 and 0.5 mg.L^{-1}, respectively (Vaiopoulou and Gikas, 2020; Xia et al., 2020). Additionally, the World Health Organisation (WHO) and the South African National Standards (SANS241) set a maximum allowable level of 0.05 mg.L^{-1} of chromium in drinking water (Ali Khan Rao et al., 2012; Nthunya et al., 2017).

The accelerated rate of industrialization, predominantly in the leather tanning, textile, electroplating, paint, and pigment production sectors, significantly contributes to the prevalence of Cr(VI) pollutants in aquatic environments (Dongre, 2021; Naja and Volesky, 2017; Guya, 2017). Innovative and contemporary water treatment technologies are available to normalize the unregulated discharge of these hazardous pollutants in water, whether from natural or anthropogenic wastewater sources (Hassan et al., 2021; Hassan et al., 2020a). Many heavy metal ion removal techniques include ion exchange, adsorbent separation, solar water evaporation, and electrochemical processes (Kordbacheh and Heidari, 2023; Koul et al., 2022). Other diverse treatment procedures include chemical precipitation, coagulation, and reverse osmosis (Saravanan et al., 2021; Elwakeel et al., 2020; Kerur et al., 2021). However, using standard procedures to remove heavy metals at low levels appears insufficient (Hassan et al., 2020b). Additionally, these methods generate chemical residues, toxic sludge, and concentrated brine, which can contaminate soil and water, disturb aquatic life, and damage the ecosystem and natural biodiversity (Manzetti and Van Der Spoel, 2015; Nishat et al., 2023).

The adsorption process, however, has the benefit of an easy and quick removal procedure; hence, it has a great potential for eliminating hexavalent chromium ions from wastewater (Chadha et al., 2022). Owing to its outstanding advantages, including high efficiency, adaptability, ease of design and operation, cost-effective regeneration, and inexpensive starting materials, adsorption technologies have attracted much interest in pollution remediation (Chadha et al., 2022; Varsha et al., 2022). For example, Rao et al. (2015) employed *Artimisia absinthium*. This medicinal plant material showed excellent adsorption in removing mutagenic Cr(VI) from aqueous solution along with Cu(II), Ni(II), and Zn(II). They achieved a Cr(VI) ions removal efficiency of 96% from their study at pH 2 (Rao et al., 2015). However, separating the adsorbent from the aqueous solution poses a challenge.

Numerous innovative adsorbents have been developed recently and functionalized with iron oxide nanoparticles (Fe$_2$O$_3$ and Fe$_3$O$_4$) to remove hazardous heavy metal ions from the human body (Hassan et al., 2020c). These iron oxide nanoparticles exhibit low toxicity, ease of synthesis, low cost, and large surface area (Subedi et al., 2019; Altun and Ecevit, 2020; Zhang et al., 2018; Neto et al., 2019). However, as adsorbents, their adsorption performance is limited due to their leaching under acidic environments and sluggish adsorption kinetics. Furthermore, due to the nano-range particle sizes of iron oxide nanoparticles, another separation step is needed to extract the adsorbent from the purified wastewater once the sorption process is complete. To overcome this challenge, polymeric matrix materials such as cellulose nanocrystals and capping agents are envisaged. Cellulose-based materials have been discovered to work well in removing impurities from contaminated water samples due to their affordability, re-usability, eco-friendliness, and highly successful surface modifications over synthetic polymers (Nishu Kumar, 2023). Thus, incorporating these novel properties is believed to enhance the removal of target pollutants (Rápó and Tonk, 2021).

The current study developed a low-cost adsorbent made of recycled pulp and paper sludge and Nylon-6 (N6) waste, modified with iron oxide nanoparticles (Fe$_3$O$_4$) and encapsulated with chitosan (CT). Cellulose nanocrystals (CNCs) were utilized since they possess a high surface caused by OH$^-$ groups and their no-range, excellent mechanical properties, non-toxicity, and desirable chemical characteristics for adsorption processes (Babaei-Ghazvini et al., 2023). N6 is a synthetic polymer with high tensile strength, durability, compatibility, and chemical resistance (Karak, 2009; Shakiba et al., 2021). These properties made it an ideal matrix material to reinforce the nanocomposite adsorbent, ensuring mechanical stability and long-term durability. The nanocomposite was modified with Fe$_3$O$_4$ nanoparticles to increase the surface area and induce magnetic properties for ease of separation, enhanced easy recovery and regeneration of the adsorbent after heavy metal ion adsorption (Liosis et al., 2021; Khan et al., 2020).

Furthermore, chitosan (CT) possesses unique properties such as high porosity, biocompatible, reusable, sustainable, and high

adsorption efficiency due to hydroxyl (−OH) and amino (−NH$_2$) groups (Sheth et al., 2021), making it an ideal capping agent to nanocomposite adsorbent. This work presents a novel method that employs waste-based materials (CNCs and N6), induced magnetic properties from Fe$_3$O$_4$ nanoparticles, and CT as a chelating agent. The novel adsorbents present excellent properties for the effective adsorption of heavy metal ions from aqueous solutions with their simple separation and recovery.

2 Materials and methods

2.1 Chemicals and reagents

Cellulose nanocrystals (CNCs) were prepared from recycled pulp and paper waste (Suter et al., 2024a; Suter et al., 2023b). Waste N6 was obtained from the Vaal University of Technology, Science Park campus-South Africa. Chitosan (C$_{56}$H$_{103}$N$_9$O$_{39}$), oxalic acid (C$_2$H$_2$O$_4$, ≥98%), hydrochloric acid (HCl ≥32%), potassium dichromate (K$_2$Cr$_2$O$_7$ >99%), sodium hydroxide (NaOH >98%), iron (III) chloride hexahydrate (FeCl$_3$.6H$_2$O, ≥99%), ammonium hydroxide (5N, NH$_4$OH, ≥25%), ferrous sulfate heptahydrate (FeSO$_4$.7H$_2$O, ≥99.5%), methanol (CH$_3$OH, ≥99.85%), molybdenum magnet and sulfuric acid (H$_2$SO$_4$, ≥99.85%), were purchased from Sigma-Aldrich, Meck-South Africa. All chemicals used were analytical grade and supplied without any further purification. The experiments were performed using deionized water from the Vaal University of Technology distillation column.

2.2 Preparation of the nanocomposite adsorbent

2.2.1 Synthesis of magnetic CNCs/ N6 nanocomposite (CNCs/N6@Fe$_3$O$_4$)

The precursor N6 solution was prepared by mixing 14.0 g of shred N6 with a formic acid and acetic (1:1) acid solution at 80°C while continuously stirring at 150 rpm until a viscous solution was obtained. Afterwards, 10.0 g of CNCs was added gently to the resulting viscous solution and agitated under the same operating conditions for 1 h. The resulting CNCs/N6 viscous solution was quenched using 10-fold deionized water, filtered, and dried overnight at 50°C. The subsequent step involved crashing the dried CNCs/N6, then sieving using double mesh sieves with mesh sizes <50 μm to get finer particles. The obtained fine particles were packed in airtight plastic sample holders for the following procedure.

The magnetized cellulose nanocrystals/nylon−6 iron oxide nanocomposite (CNCs/N6@Fe$_3$O$_4$) was prepared using a modified method described in previous work (Suter et al., 2024a; Evans et al., 2022). Briefly, in a three-neck round-bottomed flask, a mixture containing 4.5 g of CNCs/N6 and 500 mL of deionized water was vigorously stirred at 200 rpm for 1 h at 80°C. The flask was fitted with a nitrogen circulation system to maintain an inert environment. After complete dispersion of CNCs/N6, 3.1 g of FeSO$_4$.7H$_2$O and 2.1 g of FeCl$_3$.6H$_2$O were added to the 80°C preheated mixture. It was followed by adding 5 N of NH$_4$OH

dropwise while vigorously stirring until it turned dark brown. The stirring was continued for an additional 30 min. As stated in prior work (Suter et al., 2023b), the nanocomposite was collected using a molybdenum magnet and washed many times with deionized water. Finally, the resulting CNCs/N6@Fe$_3$O$_4$ nanocomposite was oven-dried for 24 h at 50°C.

2.2.2 Preparation of chitosan-encapsulated magnetic nanocomposite (CNCs/N6@Fe$_3$O$_4$−CT)

A modified method described by Sharififard and Rezvanpanah et al. (2021) and Mashile et al. (2020) was used to prepare the magnetic CNCs/N6@Fe$_3$O$_4$-chitosan nanocomposite (Mashile et al., 2020; Sharififard and Rezvanpanah, 2021). To prepare a solution of 0.2 M oxalic acid, 500 mL of deionized water was heated using a hot plate at 45°C–50°C, then gradually adding 2.5 g of chitosan while constantly stirring using a magnetic stirrer until a viscous gel formed. Then, 5.0 g of magnetized CNCs/N6@Fe$_3$O$_4$ nanocomposite was gently introduced and mixed for 2 h at 45°C–50°C and 150 rpm. After that, dropwise injections of the magnetic CNCs/N6@Fe$_3$O$_4$-chitosan mixture were made into a 0.7 M NaOH precipitation bath in order to create beads. The produced beads were filtered out of the NaOH solution and repeatedly washed with deionized water after they reached a neutral pH. The beads were ground into a fine powder and oven-dried overnight at 50°C for characterization and wastewater purification experiments.

2.3 Nanocomposite adsorbent characterization

The Fourier transform infrared spectroscopy (FTIR) analysis employed a Thermo Scientific Nicolet iS10 (Smart iTR) device with a diamond-based attenuated total reflectance (ATR) compartment was used to determine the chemical molecular structure of CNCs/N6@Fe$_3$O$_4$−CT nanocomposite adsorbent before and after synthetic water treatment together with its precursor materials. The spectral resolution was set at 4 cm^{-1} over 4,000 and 500 cm^{-1} wavelength range. An average of 16 scans were captured for each spectrum, and the primary absorption peaks were identified. Surface morphology was examined using a scanning electron microscope (JEOL-IT 7500LA, Japan) with an accelerating 15–20 kV voltage. The samples were sputtered with a thin coating of gold metal after being placed on a carbon tape metal stub, then shattered in liquid nitrogen coated with gold to see the cross-sectional morphologies. A Shimadzu-XRD 700 X-ray diffractometer with Cu Ka radiation (λ = 0.1539 nm) was used to obtain the X-ray diffraction (XRD) patterns. The parameters for the equipment were 40 kV voltage, 30 mA current, and 1 Hz scan rate. Measurements were taken and recorded after the samples were loaded into the sample holder and placed on the XRD slot. Scherer's Equation was used to calculate the crystal size (D), as indicated in Equation 1 below. This formula accounts for the X-ray wavelength (λ), the Braggs angle (θ), the dimensionless form factor (K), and the line broadening at half maximum intensity (FWHM) (β) (Monshi et al., 2012).

$$Crystal\ Size\ (D) = \frac{K\lambda}{\beta\,Cos\,\theta} \qquad (1)$$

A vibrating sample magnetometer (VSM) operating in the temperature range of 1.8–320 K and with a magnetic field of around ± 14 Tesla was used to measure the magnetic properties. The pH point zero charge (pH_{PZC}) for the Fe_3O_4, $CNCs/N6@Fe_3O_4$ and $CNCs/N6@Fe_3O_4$–CT were established using the pH drift equilibrium method. Briefly, 0.01 M NaCl stock solution was prepared, followed by 10 distinct 250 mL flasks filled with 50 mL of the solutions. The pH of the solutions was adjusted from 1 to 10 by adding 0.1 M NaOH/HCl solution dropwise, providing each flask with a distinct pH value. Each sample weighed 0.1 g and was put into different flasks with different pH values. The solutions were equilibrated for 48 h before the final pH was measured. The point of intersection was the pH_{PZC} of the prepared samples.

2.4 Batch adsorption experiments

Batch experimental studies were performed to determine the influence of various parameters, including the pH of the synthetic wastewater solution, nanocomposite adsorbent mass, metal ions concentrations, and the adsorption temperature. Hexavalent chromium solutions were made by dissolving potassium dichromate in double-distilled water. To create solutions with the necessary concentrations, a stock solution containing 1,000 mg/L was first prepared and then diluted to various solutions with different concentrations. The hexavalent ion solutions with the adsorbents under the multiple parameters to be investigated were shaken in a Merck Milipore-355 electric shaker at a 200 rpm shaking rate to attain equilibration.

The initial pH of the Cr(VI) solution adopted from preliminary results was adjusted from 1.0 to 12.0 using 0.1 M NaOH/HCl. The contact time (t) was varied from 1–150 min, starting metal ion concentrations (C_o) were set at 5–100 mg/L, with operating temperatures ranging from 298 to 318 K. The optimal pH value was used to test the effect of the adsorbent dose, with a Cr(VI) concentration of 20 mg/L and an adsorbent mass ranging from 0.025 to 0.30 g (1.0 g/L to 3.0 g/L) in 25 mL reactor.

The total Cr(VI) concentrations were measured using a Thermo Solaar S4 Atomic Absorption Spectrometer (AAS) at a wavelength of 357.9 nm under nitrous oxide using an air/acetylene flame. Before analysis, the mixtures were separated using a molybdenum magnet and filtered using Wathman No 1 filter paper. A 0.45 μm syringe filter followed this to prevent permeable particles from damaging the AAS aspirator. The obtained data was fitted to kinetics, isotherms and thermodynamics models.

The adsorbent performance was evaluated using Equations 2, 3 below to determine the amount of solute adsorbed per gram (removal capacity) of the nanocomposite (mg/g) at any time (q_t), and at equilibrium (q_e).

$$q_t = \frac{(C_o - C_t)V}{m} \qquad (2)$$

$$q_e = \frac{(C_o - C_e)V}{m} \qquad (3)$$

where V is the working solution volume (L), q_t is the quantity of solute adsorbed (mg/g), C, and C_t represent the starting concentration and concentration at any time (t) in (mg/L), m is

the mass of adsorbent, (g), and C_e is the concentration at equilibrium.

The adsorbent percentage removal efficiency (%RE) was calculated using Equation 4, where C_o represents the initial concentration and C_e represents the final concentration in milligrams per litre (mg/L).

$$RE = \frac{(C_o - C_e)}{C_o} * 100\% \qquad (4)$$

2.5 Effect of salts/electrolytes on CNCs/N6@Fe₃O₄–CT adsorption process

Process effluents comprise various monovalent, divalent, and trivalent salts/electrolytes. Thus, the nanocomposite adsorbent was investigated in the presence of NaCl, $CaCl_2$, and $FeCl_3$ at optimal parameters obtained in Section 2.4 to ascertain its noble applicability.

2.6 CNCs/N6@Fe₃O₄–CT nanocomposite adsorbent regeneration

To evaluate the re-usability of the nanocomposite adsorbent, separate 0.3 L solutions containing 20 mg/L of Cr(VI) were in contact with 0.30 g of the adsorbent for 120 min to ascertain sorption efficiency. After adsorption, the adsorbent was separated, rinsed with deionized water, and dried overnight. The loaded adsorbent was divided into three portions (0.10 g each). Each portion was then shaken using a Merck Milipore-355 electric shaker in one of the three desorption solvents: deionized water (H_2O), 0.1 M hydrochloric acid, and 0.1 M sodium hydroxide for 120 min. The supernatant solution was then filtered, and the used adsorbent was cleaned with deionized water and dried in an oven for reuse (three cycles). The Cr(VI) concentrations were analyzed in the residual solutions following adsorption and desorption experiments. Equation 5 was used to calculate the percentage efficiency of the desorption of metal ions.

$$DE = \frac{C_d}{C_a} \, x \, 100\% \qquad (5)$$

where DE is the desorption efficiency, C_d is the concentration desorbed, C_a is the concentration adsorbed.

3 Results and discussions

3.1 Adsorbent screening

3.1.1 FTIR molecular structure determination

The FTIR spectra of the precursor materials and the nanocomposite adsorbent ($CNCs/N6@Fe_3O_4$–CT) before and after adsorption are shown in Figures 1A, B. From the infra-red characterization results, Figure 1A shows the tensile, flexural, and modified vibrations for O–H, C–H, and C–O corresponding to absorption bands of cellulose nanocrystals at wavelengths
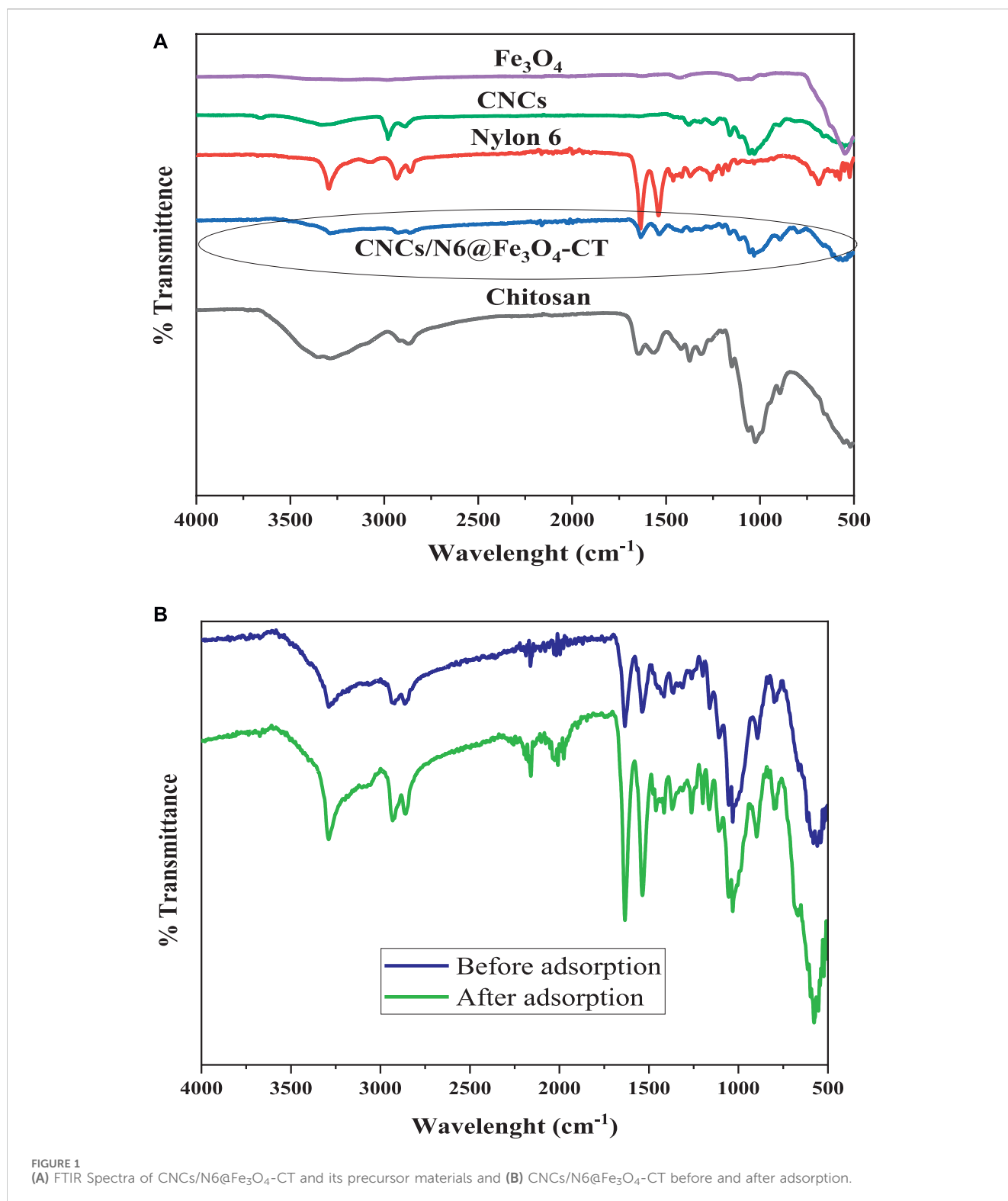
FIGURE 1
(A) FTIR Spectra of CNCs/N6@Fe$_3$O$_4$-CT and its precursor materials and **(B)** CNCs/N6@Fe$_3$O$_4$-CT before and after adsorption.

2,922.42 to 3,427.65 cm^{-1}, 1,437.45 cm^{-1}, 1,379.66 cm^{-1}, and 1,043.75 cm^{-1} respectively (Banza and Rutto, 2022; Tlou et al., 2023). Similarly, the absorption bands in N6 are linked to tensile vibrations at 3,296.17 cm^{-1}, 1,632.35 cm^{-1}, 1,537.39 cm^{-1}, 1,272.45 cm^{-1}, and 689.12 cm^{-1} corresponding to N–H stretch, C=O stretch, N–H in-plane bend, C–N stretch, and N–H out-of-plane bend (Rodríguez et al., 2021). The flexural vibrations of the

Fe–O group and the absorbed water for the Fe$_3$O$_4$ nanoparticles are linked to the absorption bands at 546.28 and 1,650.13 cm^{-1}. On the other hand, chitosan displayed absorption bands 3,229.68 cm^{-1}, 2,886.44 cm^{-1}, 1,635.10 cm^{-1}, 1,374.60 cm^{-1}, 1,021.19 cm^{-1}, and 897.99 cm^{-1}. Similar results were reported by (Smith, 2018) and are linked to various functional groups of chitosan, including O–H stretch, C–H bend, N–H bend, C–C in ring stretch, C–O stretch for
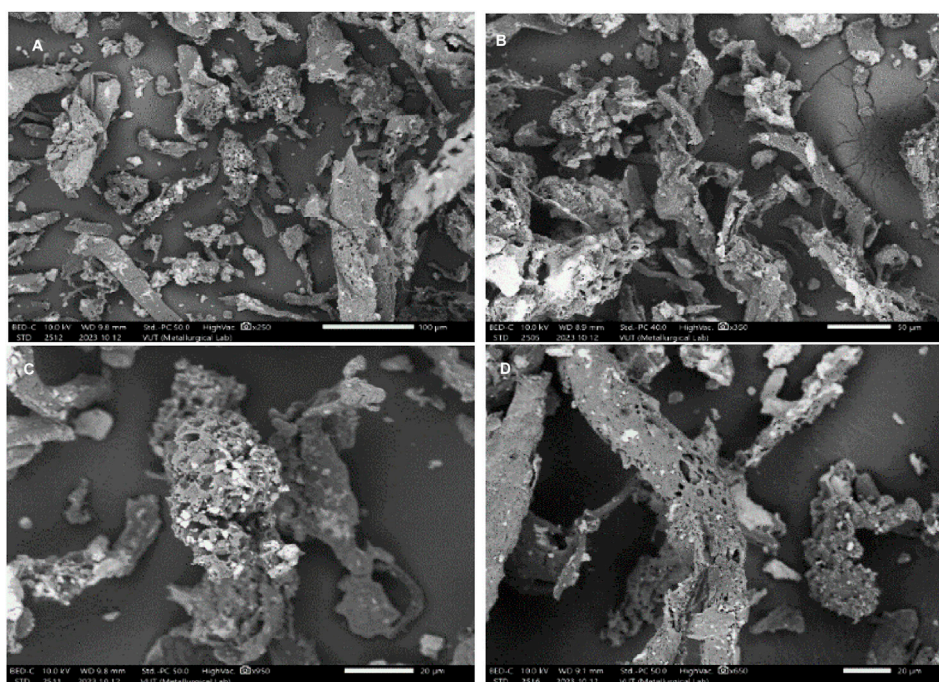
FIGURE 2
SEM micro-graphs of CNCs/N6@Fe$_3$O$_4$-CT at different magnifications; **(A)** 100 µm, **(B)** 50 µm, **(C,D)** 20 µm.
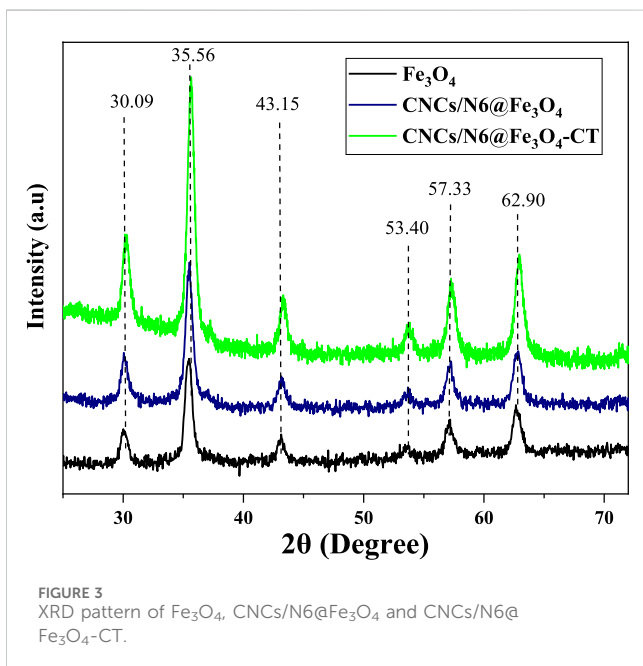
FIGURE 3
XRD pattern of Fe$_3$O$_4$, CNCs/N6@Fe$_3$O$_4$ and CNCs/N6@Fe$_3$O$_4$-CT.

incorporation into the adsorbent. Nonetheless, the functional groups shifted slightly to higher or lower wavelengths with widening/narrowing of some bands. After adsorption, it was noted that the functional groups did not undergo significant changes, as most peaks remained unaltered. This suggests that the material possesses exceptional characteristics and stability and has the potential for long-term re-usability.

3.1.2 Surface morphology

The SEM images in Figure 2 show the morphology of the produced nanocomposite adsorbent at different magnifications. It is evident from the SEM images that the nanocomposite adsorbent is composed of particles of various sizes and structures: finger-like, rod-like, flattened, string-like, spongy-like, and crystal-like structures. This suggests that the nanocomposite has a heterogeneous surface, which could contribute to enhanced surface area, porosity, and improved adsorption kinetics and adsorption capacity. Furthermore, it was observed that the adsorbent exhibits a porous surface with void patterns of varying sizes and shapes. This could imply that the nanocomposite material was successfully prepared and has a very high permeability.

3.1.3 Crystal properties

Figure 3 depicts the X-ray diffraction patterns for Fe$_3$O$_4$, CNCs/N6@Fe$_3$O$_4$, and CNCs/N6@Fe$_3$O$_4$–CT. It can be observed that the magnetite reflections (220), (311), (400), (422), (511), and (440) are the principal X-ray diffraction patterns at 2θ peaks, which are located at 30.09°, 35.56°, 43.15°, 53.40°, 57.33°, and 62.90° (Evans et al., 2022; Xu et al., 2013). These peaks correspond to JCPDS number 19–629 (Safitri et al., 2021) and suggest that the CNCs/N6@Fe$_3$O$_4$ and CNCs/N6@Fe$_3$O$_4$–CT nanocomposite incorporated the

alcohols, and N–H wag (1 and 2 amine), respectively (Claude and Onyango, 2024; Valentin et al., 2007).

Figure 1B shows most of the functional groups of precursor materials in the prepared nanocomposite. For example, the absorption bands for CNCs, N6, Fe$_3$O$_4$, and chitosan appeared in the nanocomposite at 3,282.60 cm^{-1}, 2,929.09 cm^{-1}, 2,861.26 cm^{-1}, 1,639.53 cm^{-1}, 1,537.39 cm^{-1}, 1,421.68 cm^{-1}, 1,028.27 cm^{-1}, 892.61 cm^{-1}, and 552.67 cm^{-1} respectively, indicating successful

FIGURE 4
Room-temperature magnetization curve of Fe_3O_4, CNCs/N6@Fe_3O_4 and CNCs/N6@Fe_3O_4-CT.

TABLE 1 BET surface area and pore properties.

Parameters	Adsorbents				
	CNCs	N6	Fe_3O_4	CNCs/N6@Fe_3O_4	CNCs/N6@Fe_3O_4–CT
Surface area ($m^2.g^{-1}$)	4.538	1.824	7.591	6.329	6.693
Pore volume ($cm^3.g^{-1}$)	0.0063	0.0028	0.0078	0.0031	0.0066
Average pore diameter (nm)	0.438	0.316	3.293	2.501	1.861

crystalline spinel-structured magnetite (Fe_3O_4) phase of iron oxide. The intense, distinct peaks indicate that the prepared materials were crystallized. The prepared Fe_3O_4, CNCs/N6@Fe_3O_4, and CNCs/N6@Fe_3O_4–CT had a particle size of 15.21 ± 2.91, 81.26 ± 1.56 and 103.34 ± 2.87 nm as calculated using the Scherer equation.

3.1.4 Magnetic properties

The room-temperature magnetization curve gives a superparamagnetic state. The magnetite-based adsorbents Fe_3O_4, CNCs/N6@Fe_3O_4, and CNCs/N6@Fe_3O_4–CT showed the absence of coercivity and remanence (Figure 4). The CNCs/N6@Fe_3O_4-CT adsorbent saturation magnetization was established to be 26.90 emu/g, which is much lower than that of CNCs/N6@Fe_3O_4 (53.80 emu/g) and Fe_3O_4 (68.87 emu/g). The reported values were less than those for bulk Fe_3O_4, always within 92–100 emu/g (Cornell and Schwertmann, 2003). In the CNCs/N6@Fe_3O_4 and CNCs/N6@ Fe_3O_4–CT, magnetic nanoparticles might have been "diluted" by diamagnetic physically adsorbed water, surface modifiers (CNCs, and N6), and the capping agent (CT), which significantly lowered the observed saturation magnetization. This could suggest that the capping agent and the surface modifiers may have altered the

magnetic strength. Studies further report that the tiny size of Fe_3O_4 magnetic nanoparticles contributes to the value that is less than that of bulk Fe_3O_4 (Kodama, 1999). Small nanoparticles often have lower saturation magnetization values than bulk material of the same composition due to surface effects such as a magnetically deformed surface layer (Petrinic et al., 2021).

3.1.5 Brunauer−Emmett−Teller (BET) surface properties

Brunauer–Emmett–Teller (BET) was performed to efficiently investigate the impacts of modifying materials on the adsorbents' surface area. The data in Table 1 revealed that incorporating Fe_3O_4 increased the surface area of the nanocomposite. The same scenario was also observed with further addition of the capping agent (CT). The particles' surface area was in the sequence of Fe_3O_4 >CNCs/N6@Fe_3O_4–CT > CNCs/N6@Fe_3O_4 >CNCs > N6. These findings demonstrated that adding CT and Fe_3O_4 boosted nitrogen adsorption, whereas CNCs, N6, inhibited it. The inclusion of magnetic iron oxide nanoparticles improved the nanocomposite adsorbent's surface area, which is essential when determining whether an adsorbent is appropriate for water purification
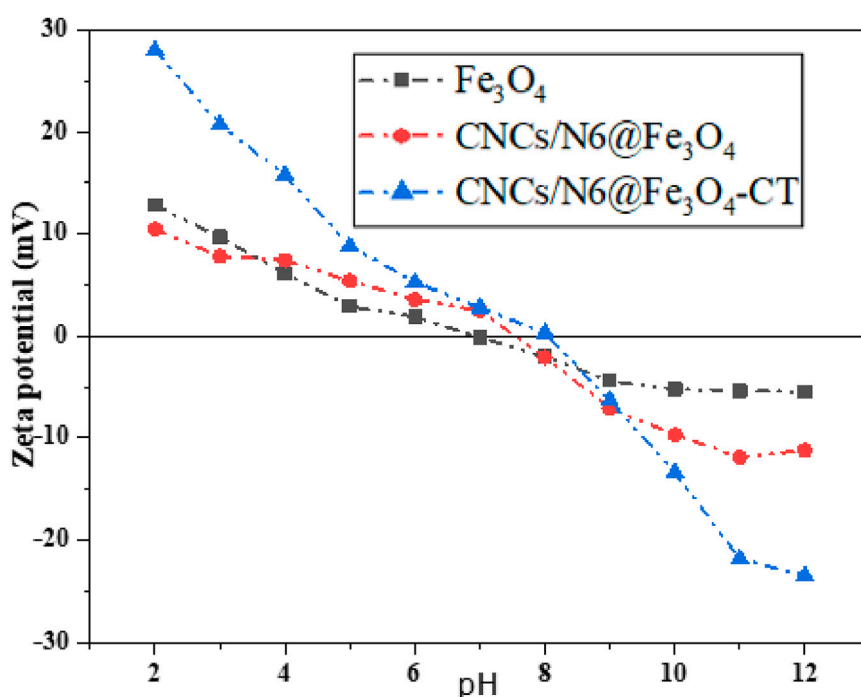
FIGURE 5
Zeta potential plot for Fe_3O_4, CNCs/N6@Fe_3O_4, and CNCs/N6@Fe_3O_4-CT

(Ayoade et al., 2020). However, the findings showed that Fe_3O_4 had wider pore openings, which were seen to narrow when incorporated into CNCs and N6. As a result, the surface pores increased when the nanocomposite was capped with CT. Consequently, even though CNCs and N6 reduced the pore sizes, the adsorbent sorption sites may still have been enhanced due to the addition of more functional groups that provide extra binding sites on the surface, as revealed by the FTIR data.

3.1.6 Zeta potential

Figure 5 illustrates zeta potential *versus* pH curves for Fe_3O_4, CNCs/N6@Fe_3O_4, and CNCs/N6@Fe_3O_4–CT. The isoelectric point (IEP) pH at zero point charge (pH_{PZC}) were found to be 6.7, 7.5 and 7.9 for Fe_3O_4, CNCs/N6@Fe_3O_4 and CNCs/N6@Fe_3O_4–CT, respectively. This is supported by research investigations by Lesiak-Orłowska et al. (2019) which concluded that when iron atoms coordinate with readily dissociable H−O−H molecules, surfaces composed of Fe_3O_4 become hydroxyl functionalized. These hydroxyl groups on the amphoteric surface react with bases or acids to create a pH_{PZC} that closely replicates neutrality. The charge on Fe_3O_4 surfaces can be positive or negative depending on the pH of the solution. When the surface is protonated below the isoelectric point, it generates $\equiv-FeOH^{2+}$, resulting in a net positive charge. However, when the surface hydroxyl groups are deprotonated, it produces $\equiv-Fe-O^-$ surface groups above the isoelectric point (Cristiano et al., 2011). The magnetic iron oxide nanoparticles are highly unstable because of their surface density charge (σ), which is too small in the IEP. This may result in the clumping of nanoparticles and flocculation. Studies from the literature indicate that the superficial charge must be altered using a variety of organic or inorganic surface modifiers to

prevent agglomerations (Favela-Camacho et al., 2019). This can be observed from the changes in IEP because of the adsorbent modification with CNCs, N6, and CT. Furthermore, the observed IEP of 7.9 for CNCs/N6@Fe_3O_4–CT is linked to the IEP of CT, which is around 7.0–9.0. Notably, integrating CT into the composite resulted in high positive values for the zeta potential (Munim et al., 2020).

## 3.2 Effect of adsorption parameters

3.2.1 Effect of pH on the hexavalent chromium adsorption

Figure 6A displays the removal capacity of the adsorbents under various pH levels. From the experimental findings, Cr(VI) removal showed an increasing sorption tendency between pH 1.0 and 2.0, followed by a gradual decline from pH 3 to 12 for all the adsorbents. Studies from the literature indicate that in aqueous solutions with a pH range of 2.0–8.5, the bulk metal ions exist as $M^{+/2+}$ or $M(OH)^+$ ions (Li et al., 2020). Most metal ions produce $M(OH)^{2+}$ above basic pH, leading to precipitation. Therefore, conducting adsorption experiments below pH 9.0 is always safe to prevent metal ion precipitation. Similarly, the concentration of H_3O^+ ions is substantially larger and exceeds that of metal ions at very low pH values. Excessive H_3O^+ ions cover the active sites of the adsorbent, allowing the metal ions to move about freely in the solution (Cruz-Lopes et al., 2021), translating to competing reactions between the adsorbate metal ion and H_3O^+ ions. As the pH of the solution becomes more basic, there is less competition, and positively charged metal ions stick to available binding sites on the adsorbent (Dhumal and Sadgir, 2023). Furthermore, pH_{PZC} is
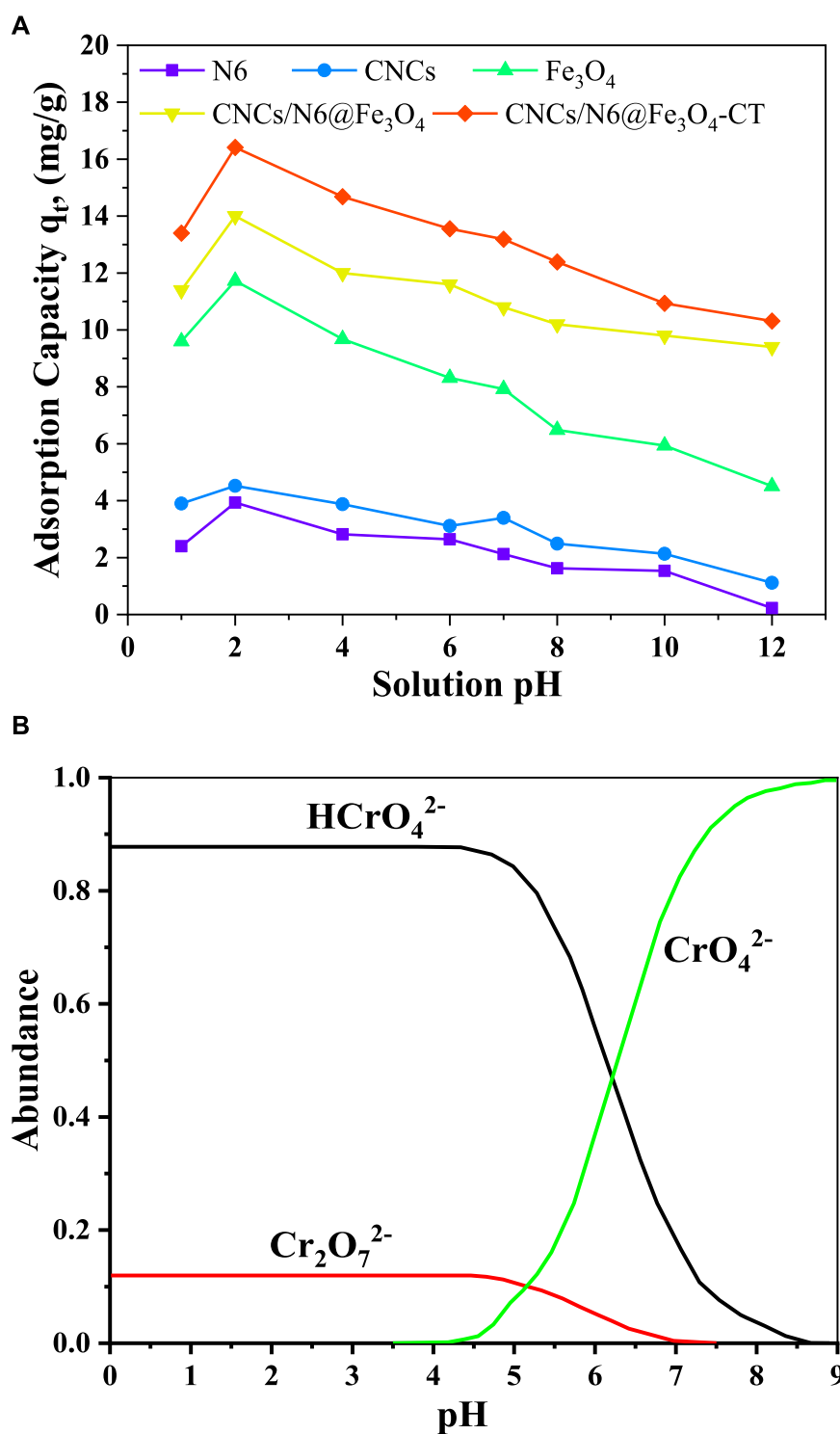
FIGURE 6
(A) Effect of solution pH on adsorption process at the optimal contact time of 120 min, initial metal ion concentration of 20 mg/L, adsorbents dosage of 1.0 g/L, shaking rate of 200 rpm at 298 K, **(B)** Stability of various hexavalent chromium species under different pH conditions.

vital in increasing adsorption capacity at high solution pH. However, this was different with Cr^{6+}, which demonstrated greater adsorption effectiveness at pH 2.0 (Figure 6A) with adsorption capacity of 3.93, 4.52, 11.72, 14.00 and 16.41 mg/g for N6, CNCs, Fe_3O_4, CNCs/N6@ Fe_3O_4, and CNCs/N6@Fe_3O_4–CT respectively.

According to the literature, the stability of various hexavalent chromium species in solution depends greatly on the pH of the solution (Ouma et al., 2022). These species include chromic acid (H_2CrO_4), hydrogen chromate ($HCrO^{4-}$), dichromate ($Cr_2O_7^2$), and chromate (CrO_4^{2-}), which are

FIGURE 7
Effect of adsorbent dosage; **(A)** Cr(VI) adsorption capacity and **(B)** Cr(VI) removal efficiency.
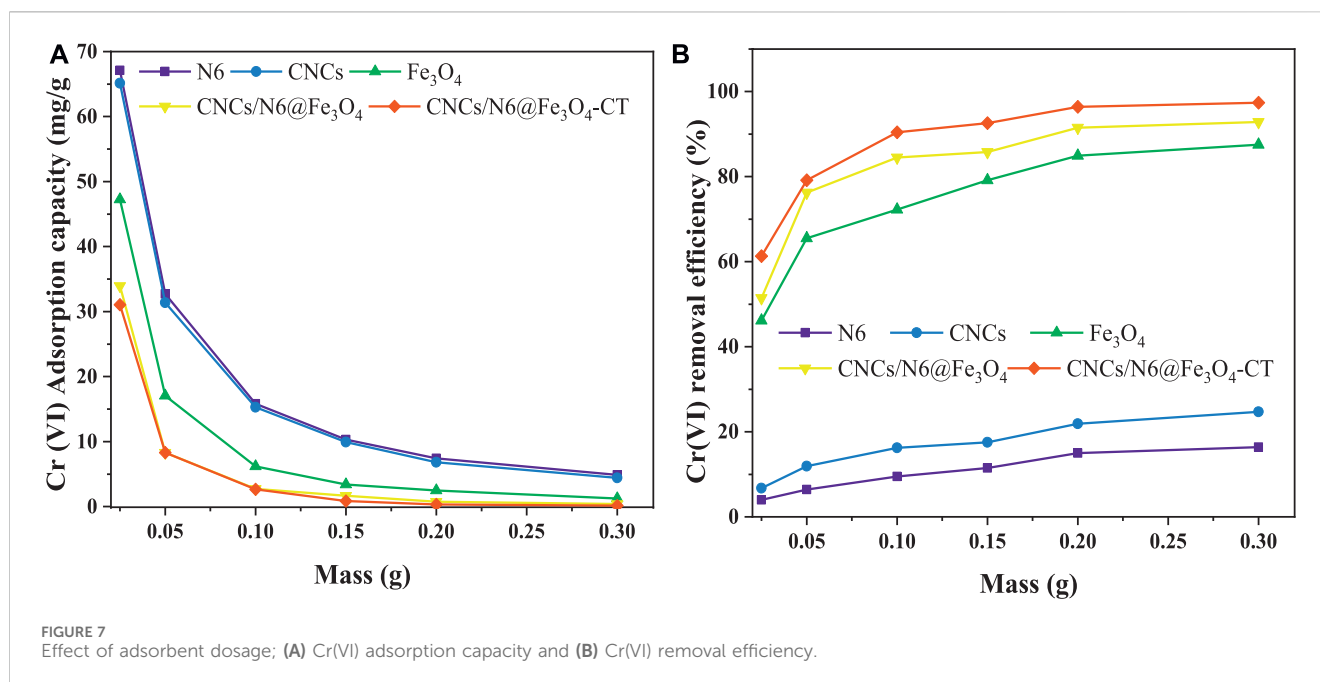
formed as the pH of the solution rises from pH 1.0–6.0 (Figure 6B) (Unceta et al., 2010). At acidic pH, the high concentration of hydrogen ions protonates the surface binding sites of the adsorbent, causing the negatively charged Cr(VI) species to be electrostatically attracted and bound to the adsorbent surface. This causes the hexavalent chromium ions to be removed from the synthetic wastewater. The ions may stay bound by electrostatic forces, or a reduction on the surface of the adsorbent may follow this sorption. The pH of 2.0 was determined to be optimal because the majority of the Cr(VI) ions in the solution were transformed to Cr(III) at pH 1.0 (Pfeifer and Skerget, 2020). Equations (6–9) below illustrate the Cr(VI) adsorption mechanisms onto CNCs/N6@Fe$_3$O$_4$–CT.

Equations 6, 7 represent the electrostatic attraction and complexation with functional groups from CNCs and N6.

$$R\text{–}OH + Cr_2O_7^{2-} \rightarrow R\text{–}O\text{–}Cr_2O_7^{2-} + H^+ \text{ (Electrostatic attraction)} \tag{6}$$

$$R\text{–}NH_2 + Cr_2O_7^{2-} \rightarrow R\text{–} NH_2.Cr_2O_7^{2-} \text{ (Complexation)} \tag{7}$$
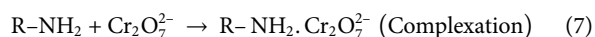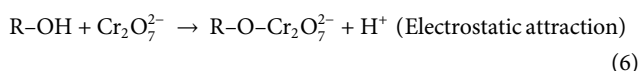
where R-represents the main matrix of CNCs/N6@Fe$_3$O$_4$–CT nanocomposite.

Equations 8, 9 represent the partial reduction of Cr(VI) to Cr(III) due to the presence of Fe$_3$O$_4$.

$$Cr_2O_7^{2-} + 14H^+ + 6e^- \rightarrow 2Cr^{3+} + 7H_2O \tag{8}$$

$$Fe_3O_4 + 8H^+ + Cr_2O_7^{2-} \rightarrow 2Fe^{3+} + Cr^{3+} + 4H_2O \tag{9}$$
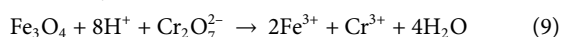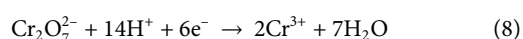
The significant improvement in adsorption capacity was due to improved surface area and a greater number of functional groups on the adsorbent surfaces due to the addition of Fe$_3$O$_4$ and CT. This is confirmed by the FTIR and BET results (Figure 1A; Table 1). The surface groups of both Fe$_3$O$_4$ and CT are amphoteric, functioning as acids or bases depending on the solution pH (Mourya et al., 2010).

3.2.2 Effect of adsorbent dosage

Adsorbent dosage is vital to adsorption since large-scale adsorption columns are designed and optimized based on adsorbent adsorption capacity. In this study, the adsorbents dosage was varied from 1.0 g/L to 3.0 g/L while the Cr^{6+} ions concentration was set at 20 mg/L, shaking speed of 200 rpm at room temperature of 298 K with optimal adsorption pH of 2.0. The findings are shown in Figures 7A, B. From Figure 7A, an apparent reduction in the adsorption capacity with an increase in adsorbent dosage was observed with all adsorbents. The obtained adsorption capacities showed a decline from 67.12 to 4.87 mg/g, 65.12 to 4.42 mg/g, 47.26 to 1.26 mg/g, 33.96 to 0.41 mg/g, and 31.06 to 0.15 mg/g for N6, CNCs, Fe$_3$O$_4$, CNCs/N6@Fe$_3$O$_4$, and CNCs/N6@Fe$_3$O$_4$–CT respectively. This is explained by the fact that there is a fixed number of potential adsorbent sites for the entire adsorption system per unit mass of total adsorbent; therefore, increasing the adsorbent's mass will probably lead to a decrease in both the amount of active sites per mass of adsorbent and adsorption capacity. In addition, increasing the adsorbent dose reduces the solute concentration difference between the surface and bulk of the adsorbent (McKinley and Jenne, 1991). Studies also reveal that the adsorbent particles interact with one another, and any system with excess solids may occasionally block potential active sites, resulting in a decreased adsorption capacity. However, as the adsorbent dosage increases, the amount of metal ions removed increases (Qasem et al., 2021). This was evident by the increased percentage removal efficiency for all adsorbents, with CNCs/N6@Fe$_3$O$_4$–CT posting a rise from 1.20% to 21.56%, 2.66%–30.54%, 35.22%–78.71%, 47.51%–89.31% and 62.97%–98.24% for N6, CNCs, Fe$_3$O$_4$, CNCs/N6@Fe$_3$O$_4$, and CNCs/N6@Fe$_3$O$_4$–CT respectively. Consequently, despite greater adsorbent doses yielding more active sites, the relationship between active sites per unit mass of adsorbent and percentage removal rate is not significant. Therefore, utilizing a smaller dosage of CNCs/N6@Fe$_3$O$_4$–CT and more concentrations of Cr(VI) ions is

FIGURE 8
Effect of initial metal ion concentration. **(A)** Cr(VI) adsorption capacity and **(B)** Cr(VI) removal efficiency.
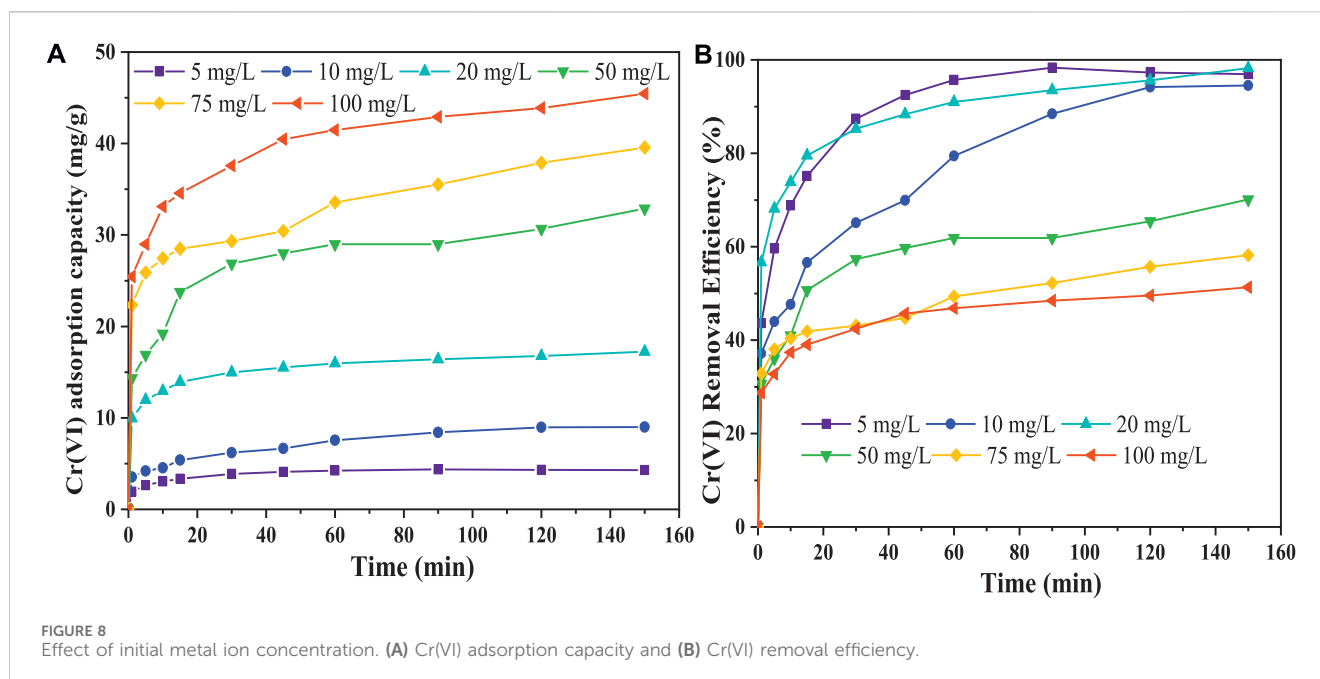
recommendable for improved removal capacity. The prepared adsorbent CNCs/N6@Fe$_3$O$_4$–CT was thus selected for optimization with increased Cr(VI) ion concentration.

3.2.3 Effect of initial Cr(VI) concentration adsorption using CNCs/N6@Fe$_3$O$_4$–CT

In this section, the working concentrations of Cr(VI) ions were 5, 10, 20, 50, 75, and 100 mg/L. The other experimental variables were set at predefined conditions: room temperature (298 K), pH of 2.0, shaking rate of 200 rpm, 150 min contact time, and adsorbent dosage of 1 g/L. Figures 8A, B) shows the adsorption capacity profile plots at different adsorbent concentrations. The findings showed an enhanced adsorption capacity from 4.31 mg/g to 45.43 mg/g as the hexavalent chromium concentrations increased from 5 to 100 mg/L (Figure 8A). The adsorbent removal rate was rapid within the first 30 min, increased sharply to around 90 min, and then gradually stagnated after approaching equilibrium at 120 min (Figure 8A). The rapid sorption of the nanocomposite adsorbent could have been attributed to adsorbent's hydrophilicity, conformational flexibility of various functional groups, larger surface area, and a more significant number of exchange sites, which are seen to decrease with time. Studies from the literature reported that the initial higher rate results from more sorption and binding sites being available on the adsorbent surface (Burtch et al., 2014). At the more reactive sites, metal ions are adsorbed, and the adsorption process grows more complex, making the sorption process less favourable as these sites are gradually occupied. Additional studies in the literature have confirmed that the adsorption of metal ions conforms to these general characteristics (Ugbea et al., 2020).

Furthermore, the studies indicate that concentration gradient roses with an increase in the initial metal ion concentration, which improves adsorption, but mass transfer resistance decreases removal efficiency (Rudi et al., 2020). From this study (Figure 8B), the CNCs/N6@Fe$_3$O$_4$–CT ability to remove Cr(VI) ions was reduced since there was greater competition among the excess Cr(VI) ions to adhere to an adsorbent surface. This can be confirmed by the decrease in removal efficiency from 98.95% to 43.60% when the initial metal ion concentration was increased from 5 mg/L to 100 mg/L.

3.2.4 Effect of system temperature on adsorption of Cr(VI) ions using CNCs/N6@Fe$_3$O$_4$–CT

The effect of temperature on the adsorption of Cr(VI) ions using CNCs/N6@Fe$_3$O$_4$–CT was evaluated at a contact time of 120 min, initial Cr(VI) concentration of 20 mg/L, adsorbent dosage of 1.0 g/L, shaking rate of 200 rpm, and a pH 2.0. The findings in Figure 9 obtained adsorption capacity of 15.10, 16.21, 16.84, 17.02, and 17.04 mg/g, while the adsorption efficiency was 81.71%, 87.70%, 91.13%, 92.07%, and 92.23% at 298 K, 303 K, 308 K, 313 K and 318 K respectively. The adsorption capacity and efficacy of Cr(VI) ions removal by CNCs/N6@Fe$_3$O$_4$–CT were positively impacted by temperature but with a minimal difference. These findings suggest that a significant amount of Cr(VI) ions may be removed using the CNCs/N6@Fe$_3$O$_4$–CT nanocomposite at room temperature. These results agree with studies from the literature, which indicated that the adsorption of metal ions using biomass and iron-based adsorbents is minimally influenced by system temperature (Ogunlalu et al., 2021).

3.3 Adsorption kinetics and mechanism of adsorption

Comprehending the kinetic interactions in adsorption reactions is essential in identifying rate-controlling steps. This understanding helps explain the factors that influence molecular interactions, such as the molecules' molecular morphology, reaction temperature, and polarity. It also enables the prediction of system functionality under various reaction environments and during scale-up procedures. The mathematical expressions employed in this study adopted linear models of the Pseudo-first-order (PFO), Pseudo-second-order (PSO), Elovich, and Intra-particle diffusion models.
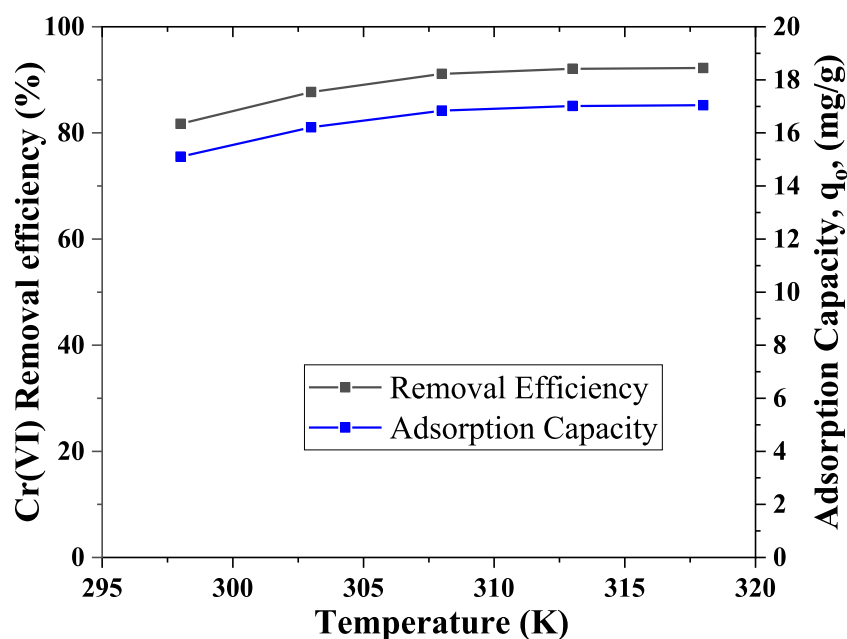
FIGURE 9
Effect of temperature on hexavalent chromium removal.
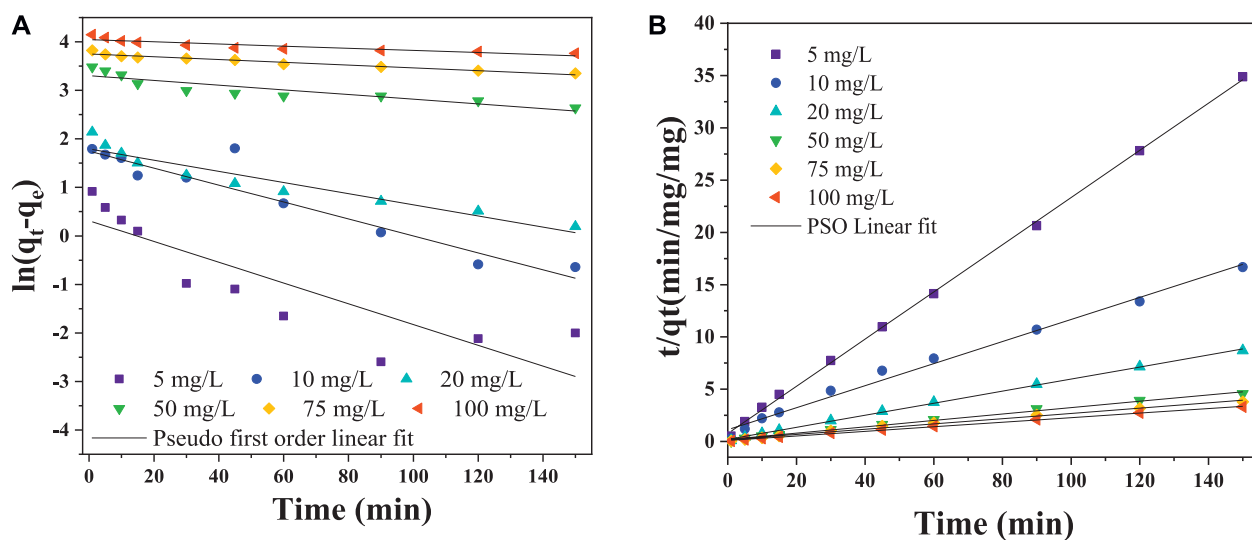
FIGURE 10
(A) Pseudo-first-order kinetic model linear fit and **(B)** Pseudo-second-order kinetic model linear fit for Cr[6+].

3.3.1 PFO kinetic model

The PFO was used to evaluate the kinetic behaviour and comprehend the Cr(VI) interaction mechanism with CNCs/N6@Fe$_3$O$_4$–CT nanocomposite adsorbent. PFO linear fit findings are presented in Figure 10A and Table 2. The generalized integral nonlinear form of the PFO kinetic model can be stated as per Lagergren, 1898 as provided in Equation 10.

$$\frac{dq_t}{dt} = K_1 (q_e - q_t) \tag{10}$$

By integrating Equation 10 at the boundary conditions, t = 0, q_t = 0, and at t = t (>0), q_t = q_t, the linear form Illustrated in Equation 11 is obtained.

$$ln(q_e - q_t) = ln\, q_e - K_1 t \tag{11}$$

where q_t and q_e variables represent the quantities of solute adsorbed at any time (t) and the amount adsorbed at equilibrium time (t) in (mg/g), K_1 reflect the first-order rate constant (min^{-1}), and t is the contact time (min). The theoretical value of q_e and the rate constant K_1 are obtained from the slope and intercept of the linear plot of $(q_e - q_t)$ vs. t.

TABLE 2 Summary of kinetic model parameters.

Kinetic model/Adsorbate	Parameters					
	5 mg/L	10 mg/L	20 mg/L	50 mg/L	75 mg/L	100 mg/L
Pseudo-first kinetic model						
q_e (exp) (mg/g)	4.361	8.426	16.412	28.983	35.509	42.912
q_e (model) (mg/g)	4.234	7.897	15.028	27.671	34.280	41.117
K_1 (mg/g)	0.0214	0.0175	0.0115	0.0048	0.0029	0.0022
R^2	0.781	0.922	0.913	0.809	0.915	0.807
Pseudo second kinetic model						
q_e (model) (mg/g)	4.154	7.3043	15.419	26.881	34.114	40.986
K_2 (g/mg.min)	0.2257	0.1055	0.0577	0.0305	0.0252	0.0219
X	0.1207	0.9216	0.7800	0.4087	0.8754	1.0025
R^2	0.9997	0.9902	0.9977	0.9954	0.9921	0.9984
Elovich kinetic model						
α (mg/g)	0.0408	0.0635	0.1101	0.1554	0.1510	0.2013
β (model)	0.5242	1.218	1.4800	3.866	3.2964	4.1937
R^2	0.9845	0.9768	0.9980	0.9763	0.9801	0.9913
Intraparticle kinetic model						
K_{id} (mg/g.min$^{0.5}$)	0.1986	0.5232	0.5805	0.5489	1.4269	1.6888
C	2.3678	3.1541	10.9162	10.3182	22.0714	26.7617
R^2	0.8981	0.9899	0.9424	0.9416	0.9902	0.9611

From the model fit, the linear regression coefficients (R^2) were comparatively low and ranged from 0.781 to 0.922; this indicated that the model was inappropriate in predicting the current adsorption mechanism Cr(VI) onto CNCs/N6@Fe$_3$O$_4$–CT nanocomposite adsorbent. The weak linear regression coefficient (R^2) and extremely low values of q_{cal} provide more confirmation of the model's failure.

3.3.2 PSO kinetic model

The findings on the applicability of the pseudo-second-order kinetic model for the study are presented in Figure 10B and Table 2. Equation 12 represents the Pseudo–second–order nonlinear kinetic mathematical expression.

$$\frac{dq_t}{dt} = K_2 \left(q_e - q_t \right)^2 \tag{12}$$

By integrating Equation 12 above, the linearized form is provided in Equation 13.

$$\frac{t}{q_t} = \frac{1}{K_2 q_e^2} + \frac{t}{q_e} \tag{13}$$

The slope $\frac{1}{q_t}$ and the intercept $\frac{1}{K_2 q_e^2}$ is obtained by plotting $\frac{t}{q_t}$ vs. t while the theoretical value of q_e (mg/g) and the second-order rate constant K_2 (g/mg.min) is determined from the slope and intercept. Additionally, Equation 14 provides the initial sorption (h) rate value at $t \to 0$.

$$h = K_2 q_e^2 \tag{14}$$

For validation of the models with the experimental data, an error function (χ) can be determined using Equation 15 below.

$$\chi^2 = \sum \frac{\left(q_e \left(exp \right) - q_e \left(calc \right) \right)^2}{q_e \left(calc \right)} \tag{15}$$

The suitability of the kinetic model on the adsorption of Cr(VI) using CNCs/N6@Fe$_3$O$_4$–CT was assessed using the linear regression coefficient (R^2) and the error function (χ). The experimental data under various physio-chemical conditions fitted well to the PSO linear kinetic model. The model displayed high linear regression coefficient values ($R^2 > 0.995$). In addition, the error function's low amplitude demonstrated the model's suitability. This confirms that electron sharing between the solute and adsorbent occurred (Equations 6–9).

Furthermore, since there was less competition between the metal ions and the adsorption site at the higher initial concentration, lower K_2 values were obtained. Numerous studies on the removal of heavy metals, including zinc (Zn^{2+}), copper (Cu^{2+}), and nickel (Ni^{2+}), demonstrated that adsorption systems followed PSO kinetics models (Biswas et al., 2019; Singh and Mishra, 2022; Singh and Mishra, 2021). The results from this study further suggest that the process is not governed by a single-step metal ion adsorption on the

FIGURE 11
Elovich kinetic model linear fit.

FIGURE 12
Intraparticle diffusion kinetic model linear fit.
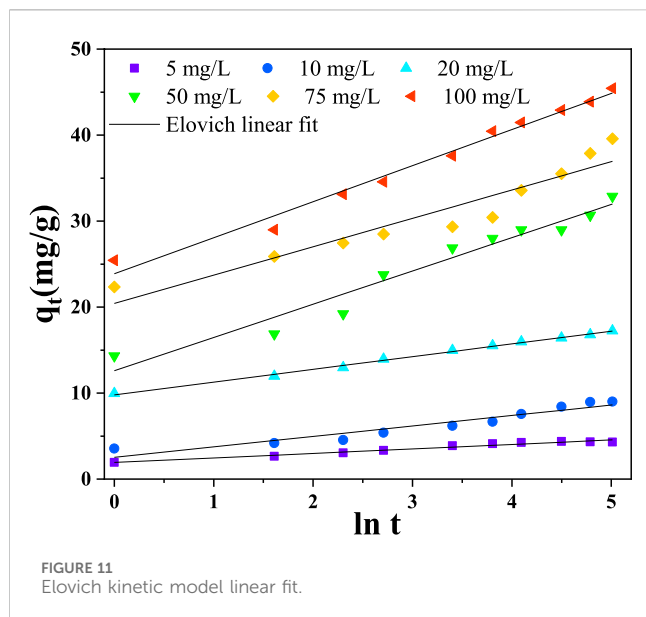
CNCs/N6@Fe$_3$O$_4$−CT nanocomposite adsorbent, and that entails several steps. These results agree with the findings reported by Salehi et al. (2021).

3.3.3 Elovich model

The kinetics of chemisorption on heterogeneous adsorbents is evaluated using the Elovich model. The model predicts the existence of heterogeneous active surface sites with various activation energies (Wang and Guo, 2023). The Elovich model is described by Equation 16, where α (mg.g^{-1}min^{-1}) is the rate of chemisorption at zero coverage, and β (g.mg^{-1}) is the desorption constant.

$$q_t = (\beta \mathrm{ln} t + \beta\, ln\, \alpha) \qquad (16)$$

The linearized form of the Elovich mathematical expression is given in Equation 17.

$$q_t = \frac{1}{\beta} \ln\left(1 + \alpha\beta t\right) \qquad (17)$$

Figure 11 and Table 2 illustrate how the model's linear fit to the experimental data permitted the derivation of the Elovich constants and linear correlation coefficient. The plot of q_t vs. ln(t) yields a linear relationship with a slope of (1/β) and an intercept of (1/β) ln (αβ). According to the Elovich model's coefficient of determination, sorption onto the CNCs/N6@Fe$_3$O$_4$−CT nanocomposite adsorbent was chemically guided as shown in (Equations 6–9) since $R^2 > 0.96$. Similarly, high initial sorption rates compared to corresponding desorption constants suggested that the nanocomposite adsorbent effectively adsorbed the metal ions (Chaudhary et al., 2019). In the Elovich model, active surface sites are assumed to be heterogeneous and to have a range of activation energies. The adsorbents had initial sorption rates alpha that were greater than the desorption constant beta, implying that it is suitable for the adsorption of metal ions. This is in agreement with studies reported in the literature (Rani et al., 2022).
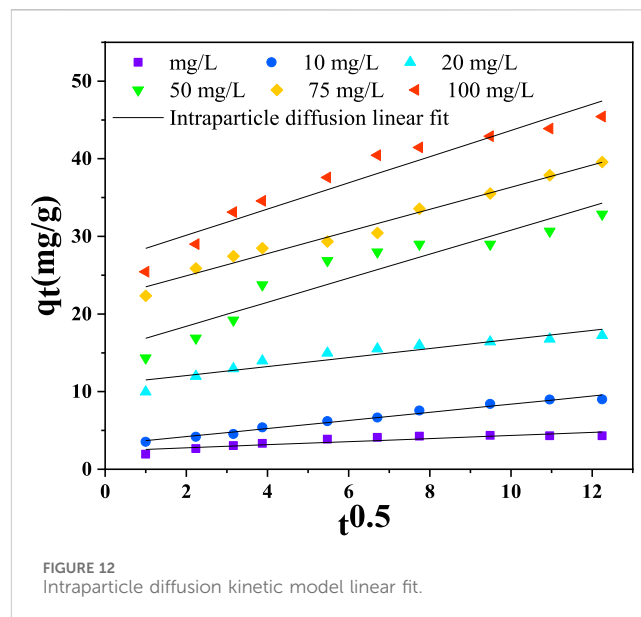
3.3.4 Intra-particle diffusion model

The intraparticle diffusion model (Webber-Morris model) is crucial for understanding the behaviour of any adsorption process (Weber and Morris, 1963; Lesiak-Orłowska et al., 2019; Ouma et al., 2022). Understanding the adsorption mechanism and how it underlies the system's apparent dynamic behaviour is essential for designing and controlling any large-scale adsorption system. The rate-limiting phases or mechanisms of the adsorption process can be identified using this model. The model's mathematical form is given in Equation 18.

$$q_t = K_{id}t^{1/2} + C \qquad (18)$$

where q_t is the amount of solute adsorbed at any time, t, (mg/g), $t^{0.5}$ is the square root of time ($min^{0.5}$) and K_{id} in (mg/g.min$^{0.5}$) is the intraparticle diffusion coefficient, respectively. The linear plot of q_t against $t^{0.5}$ yields the slope (K_{id}) and intercept (C).

According to the results of this study, as shown in Figure 12; Table 2, the hexavalent chromium ions were initially adsorbed quickly until saturation. The rate-limiting step is frequently predicted using this model for an adsorption system involving porous materials. The model states that an entire system is controlled by intraparticle diffusion when the plot between q_t and $t^{0.5}$ results in a straight line that goes through the origin. However, the plot in this study did not result in a single straight line passing through the origin. From the linear plot (Figure 12), the following steps may be listed as the adsorption mechanism: metal ion transport from the bulk solution to the adsorbent surface; diffusion across the adsorbent surface's boundary layer; adsorption on the adsorbent surface's active site and through intra-particle diffusion into the adsorbent's pores. In addition, the slowest step, external film diffusion, or pore diffusion, regulates the total adsorption rate. Studies from the literature reveal that in most situations, external film diffusion can heavily influence the entire adsorption process (Pholosi et al., 2020).

3.4 Isotherm studies

Isotherm studies predict the interactions between adsorbate molecules and the active sites on the sorbent surface. Furthermore, it offers helpful information regarding the quantity of adsorbate removed and the concentration of adsorbate at equilibrium. In technical applications such as water treatment systems, a thorough understanding of the behaviour of adsorbates and adsorbents is critical. In this study, the performance of CNCs/N6@Fe$_3$O$_4$–CT on the adsorption of Cr(VI) ions was predicted by the Langmuir, Freundlich, Temkin, and Dubinin–Radushkevich (D–R) linearized isotherm models. The coefficient of determination (R^2) was used to assess the models' superiority in predicting the adsorption of Cr(VI) ions onto CNCs/N6@Fe$_3$O$_4$–CT nanocomposite adsorbent.

3.4.1 Langmuir isotherm model

The Langmuir isotherm model assumes that the rate-limiting reaction step is a surface reaction with the same adsorption activation energy at each active site, comparable to heterogeneous catalytic reactions. Furthermore, the model presupposes that the metal ions and previously adsorbed molecules would not interact in any way (Langmuir, 1918). Equation 19 below provides the Langmuir mathematical expression in its non-linearized version.

$$q_e = \frac{q_m K_L C_e}{1 + K_L C_e} \tag{19}$$

Equation 20 shows the linearized form of the Langmuir isotherm mathematical model.

$$\frac{1}{q_e} = \frac{1}{q_m K_L C_e} + \frac{1}{q_m} \tag{20}$$

Where q_m is the maximum adsorption capacity of the adsorbent (mg/g), and K_L is the energy of adsorption (L/mg).

A straight line with a slope of $\frac{1}{q_m}$ and an intercept of $\frac{1}{K_L}$ is produced by plotting $\frac{1}{q_e}$ vs. $\frac{1}{C_e}$. This isotherm also yields the dimensionless separation factor, R_L, which determines if the adsorption process is viable at various starting solute concentrations (Abate et al., 2020). The separation factor for the dimensionless parameter may be computed using Equation 21 below.

$$R_L = \frac{1}{(1 + K_L C_o)} \tag{21}$$

If ($R_L > 1$ or $R_L = 1$), then the system is unfavourable but considered favourable if (0< R_L <1). Furthermore, $R_L = 1$ and when $R_L = 0$ describe a linear and irreversible system, respectively.

From the graphical plots (Figure 13), the Langmuir model better predicted the adsorption of Cr(VI) ions onto CNCs/N6@Fe$_3$O$_4$–CT nanocomposite adsorbent with a coefficient of determinant R^2 > 0.99, as shown in Table 2. This suggested that the monolayer adsorption process proceeded on the homogeneous surface of the adsorbent. The dimensionless separation factor R_L values calculated were within the expected range of 0< R_L <1 (0.835–0.920), thus confirming that the adsorption process was favourable.

3.4.2 Freundlich isotherm model

According to the Freundlich isotherm model, multilayer adsorption occurs on the adsorbent's heterogeneous surface. The
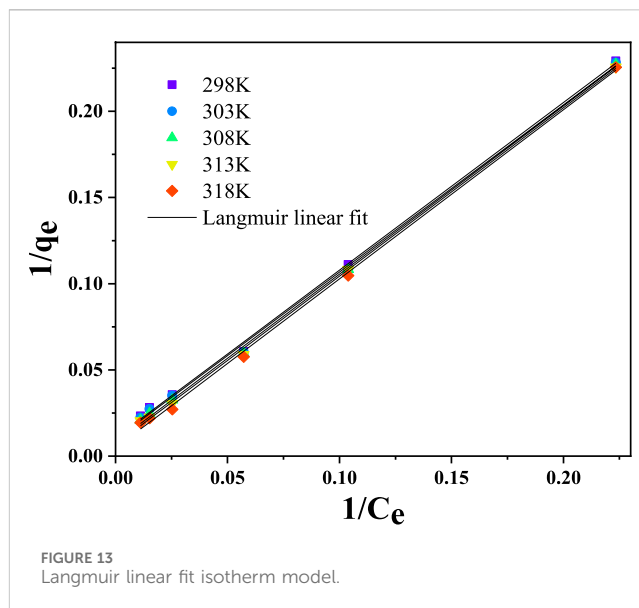
FIGURE 13
Langmuir linear fit isotherm model.

model also predicts that as the concentration of metal ions is increased, the quantity of the metal ions adsorbed increases (Freundlich, 1906). The nonlinear mathematical expression of the isotherm model is illustrated in Equation 22 below.

$$q_e = k_f t^{1/n} \tag{22}$$

The linearized form of the Freundlich isotherm model is shown below in Equation 23.

$$ln q_e = \frac{1}{n} ln C_e + ln K_f \tag{23}$$

Where C_e is the concentration of metal ions at equilibrium (mg/L), q_e is the quantity of solute adsorbed at equilibrium (mg/g), while K_f and n are Freundlich constants. The plot of $ln q_e$ *versus* $ln C_e$ results in a straight line with the slope ($\frac{1}{n}$), n is the degree of system heterogeneity) and an intercept (K_f) is the system's adsorption capacity. For favourable adsorption, n should be greater than 1.

From the study's findings in Figure 14, the Freundlich isotherms linear fit plot produced a straight line. The graphical representation demonstrates that the Freundlich model has a linear regression value (R^2 > 0.98), as given in Table 3. The results showed that multilayer adsorption of Cr(VI) ions onto CNCs/N6@Fe$_3$O$_4$–CT occurred due to the relatively high regression coefficient. Studies indicate that the adsorption process on a nanocomposite adsorbent is effective if the Freundlich constant(n) value is between 1 and 10 (Sadegh et al., 2018). According to the experimental data in Table 3, the Freundlich constants ranged from 3.8366 to 4.7043, which is within an acceptable range and suggests that the adsorption process was effective, thus making the nanocomposite adsorbent a good choice for metal ions adsorption.

3.4.3 Temkin isotherm model

The Temkin isotherm assumes a linear rather than a logarithmic reduction in the heat of adsorption, disregarding deficient and very high concentrations. The model also assumes a homogeneous distribution of bonding energy up to a specific maximum bonding energy and that the interactions between the adsorbent and metal ions would result in a
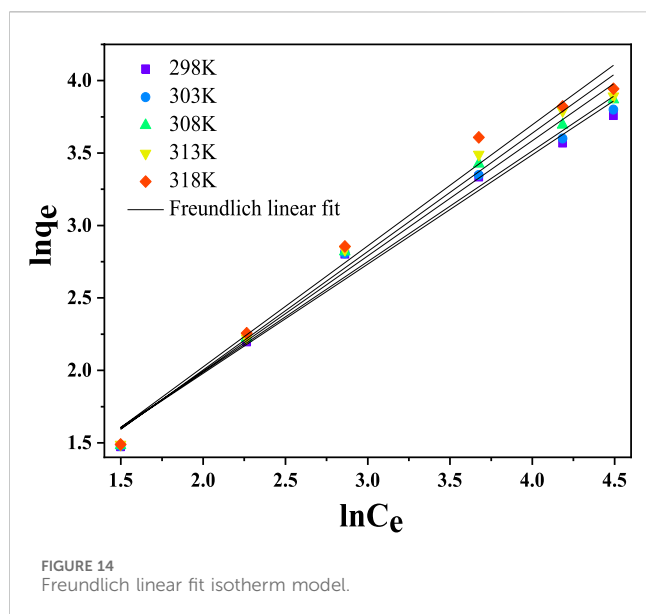
FIGURE 14
Freundlich linear fit isotherm model.

linear decrease in the heat of adsorption with surface coverage. (Temkin, 1941). Equation 24 provides the mathematical expression for the Temkin isotherm model.

$$q_e = \frac{RT}{B}lnK_T + \frac{RT}{B}lnC_e \qquad (24)$$

The linearized form of the Temkin isotherm is given below in Equation 25.

$$q_e = \frac{RT}{B}lnK_TC_e \qquad (25)$$

where B is the Temkin constant related to the heat of adsorption (J.mol^{-1}), T is the absolute temperature (K), R is the gas constant (8.314 J/mol K), and K_T is the equilibrium binding constant corresponding to the maximum binding energy (L/mol). The plot of qe vs. ln (C_e) results in a straight line with slope (RT/B) and intercept (RT lnK$_T$)/B.

From Figure 15, the interaction between the Cr(VI) ions and CNCs/N6@Fe$_3$O$_4$–CT nanocomposite adsorbent was moderate to strong. This could have been attributed to the intense heat of adsorption as indicated by the B values ranging from 3.5483 to 5.0568 J/mole. The linear correlation coefficient ($R^2 > 0.96$) further demonstrated the strong interaction, indicating that the model fitted the experimental data. The adsorption energy recorded (E < 8.0 J/mole) and high R^2 value suggest that the Temkin isotherm is a suitable model for describing the adsorption process of Cr(VI) ions onto CNCs/N6@Fe$_3$O$_4$–CT nanocomposite adsorbent. This further indicates intense contact between Cr(VI)ions and the surface of the nanocomposite adsorbent.

3.4.4 The Dubinin–radushkevich (D–R) isotherm model

The D–R isotherm model was developed to determine the typical porosity and the apparent free energy of adsorption. The isotherm model, however, does not assume a uniform surface or a constant sorption potential (Adewumi et al., 2012). It makes it possible to differentiate between chemisorption and physisorption. The Dubinin–Radushkevich isotherm, Equation 26, provides a

three-parameter equation to describe data on solute adsorption on heterogeneous surfaces.

$$q_e = q_s e^{-K_{ad}\varepsilon^2} \qquad (26)$$

where q$_s$ is the theoretical isotherm saturation capacity (mg. g^{-1}), K$_{ad}$ is a constant related to the free energy of adsorption per mole adsorbate (mol^2. J^{-2}), ε is the Polany potential associated with the equilibrium concentration (Equation 27), R is the gas constant 8.314 in kJ/mol.K, T is the temperature in Kelvin. C$_e$ is the equilibrium concentration in solution (mg/L).

$$\varepsilon = RTln\left(1 + \frac{1}{C_e}\right) \qquad (27)$$

The combination of Equations 26, 27 yields a linearized form, as given in Equation 28 below.

$$lnq_e = lnq_{max} - K_{ad}\varepsilon^2 \qquad (28)$$

where q_e is the number of ions adsorbed in (mg/g), q_{max} is the capacity of the D–R monolayer (mg/g), K_{ad} is the energy constant in (mol^2/kJ^2).

From the plot of $ln\,q_e$ versus ε^2, the slope K (mol^2/kJ^2) is obtained while q_{max} (mg/g) yields the intercept, which represents the adsorption capacity (Figure 16).

The energy required to remove each molecule of metal ion from the solution to the adsorption site can be calculated using Equation 29.

$$E = \frac{1}{\sqrt{2K_{ad}}} \qquad (29)$$

The values of mean free energy (E) are used to predict the adsorption mechanisms. When the E is ≤8 kJ/mol, it suggests a physical adsorption interaction, whereas a value E between 8 and 16 kJ/mol suggests an ion exchange mechanism. The present study's numerical adsorption values were between 10.00 and 10.660 kJ/mol, corresponding to the chemical process (Table 3). This supports the adsorption mechanisms of Cr(VI) onto CNCs/N6@Fe$_3$O$_4$–CT nanocomposite adsorbent provided in Equations 6–9.

3.5 Adsorption thermodynamics and nature of adsorption

In adsorption thermodynamics, system characteristics such as the Gibbs free energy change (ΔG^o) (kJ/mole), enthalpy change (ΔH^o) (kJ/mole), and entropy change ΔS^o (J/mol.K) are crucial in determining the energy state (exothermic or endothermic process), the degree of reaction disorder and spontaneity (Al-Harby et al., 2021; Saha and Chowdhury, 2011). Equations 30–33 below provide mathematical expressions for various thermodynamic parameters.

$$K_c = \frac{q_e}{C_e} \qquad (30)$$

$$\Delta G^o = -RTlnK_c \qquad (31)$$

$$\Delta G^o = \Delta H^o - T\Delta S^o \qquad (32)$$

$$ln\,K_c = \frac{\Delta S^o}{RT} - \frac{\Delta H^o}{RT} \qquad (33)$$

where T is the temperature in kelvin (K), R is the universal gas constant (8.314 J/mol.K), q_e is the solid-phase equilibrium

TABLE 3 Summary of isotherms and thermodynamic model parameters.

Isotherms/Adsorbate	Parameters				
	298 K	303 K	308 K	313 K	318 K
Langmuir isotherm					
q_m (mg/L)	17.4804	17.3361	16.765	17.879	18.581
K_L (L/mg)	0.0107	0.0098	0.0080	0.0067	0.0047
R^2	0.9993	0.9993	0.9996	09,996	0.9993
R_L	0.835	0.847	0.871	0.890	0.920
Freundlich isotherm					
n	3.8366	3.92494	4.2634	4.5653	4.7043
K_f	2.7883	2.8934	2.6562	2.2878	1.8656
R^2	0.9911	0.9922	0.9935	0.9931	0.9909
Temkin isotherm					
B (J/mol)	3.5483	3.9854	4.5406	4.8556	5.0568
K_T (L/mg)	1.0640	1.1948	1.3612	1.4556	1.5193
R^2	0.9868	0.9846	0.9835	0.9834	0.9840
Dubinin–Radushkevich isotherm					
K_{ad}	0.0047	0.0046	0.0046	0.0045	0.0044
E	10.314	10.425	10.245	10.541	10.660
ε (mol^2/J^2)	3.7054	3.7368	3.8065	3.8871	3.9633
R^2	0.9743	0.9695	0.9671	0.9655	0.9810
Thermodynamic parameters					
ΔH^o (kJ/mole)	−826.521	–	–	–	–
ΔS^o (kJ/mole)	2.585	–	–	–	–
ΔG^o (kJ/mole)	−1,596.85	−1,609.78	−1,622.7	−1,635.63	−1,648.55

FIGURE 15
Temkin isotherm linear fit.

FIGURE 16
Dubinin–Radushkevich Linear fit isotherm model.
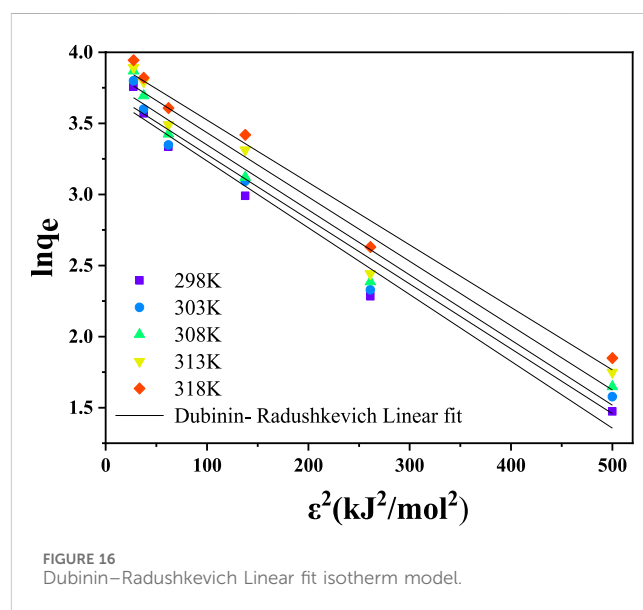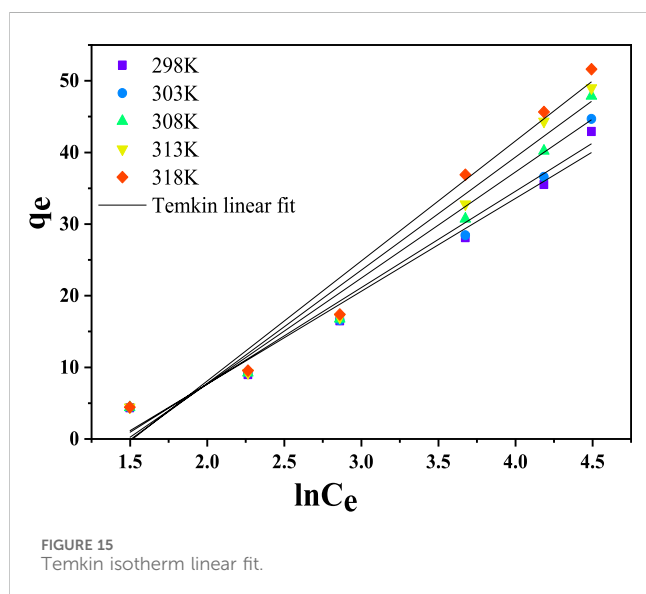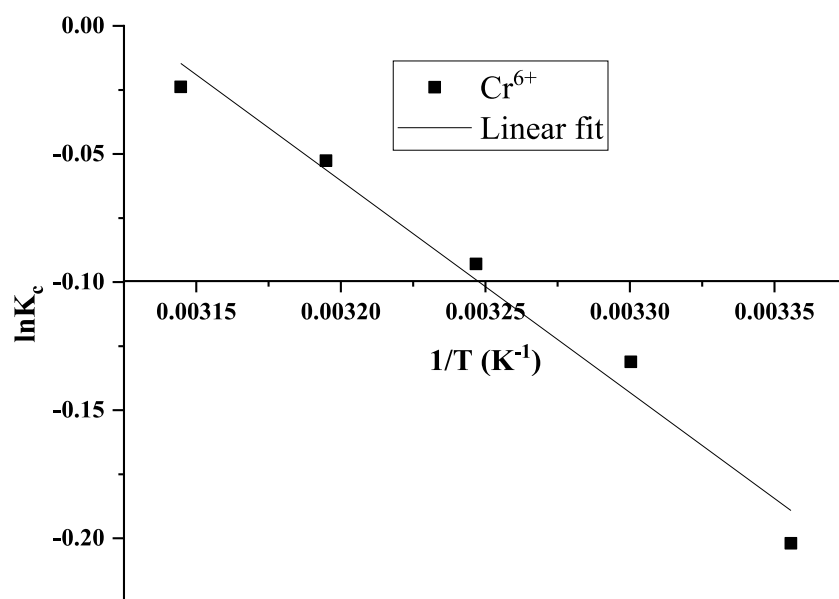
FIGURE 17
Adsorption thermodynamic plot.

concentration (mg/L), and C_e is the equilibrium solution concentration (in mg/L). The values of $\Delta H°$ and $\Delta S°$, are obtained from the slope and the intercept from the linear plot of ln (K_c) vs. $1/T$ (K^{-1}).

If $\Delta G°$ < 0, the adsorption process is said to be thermodynamically favoured; if $\Delta H°$ is negative, the adsorption process is exothermic and spontaneous, and if $\Delta S°$ is positive, it indicates increasing randomness at the solid solution interface during adsorption.

From Figure 17 and Table 3, the thermodynamic findings suggest that Cr(VI) adsorption onto CNCs was favourable with $\Delta G°$(−1,596.85 kJ/mole). It also revealed a spontaneous adsorption process with negative $\Delta H°$ values, implying that it may occur without requiring extra energy. The adsorption was exothermic, as shown by the negative value of $\Delta H°$ (−826.521 kJ/mole). Furthermore, the positive value of $\Delta S°$ (2.585 kJ/mole) demonstrated the CNCs/N6@ Fe_3O_4−CT affinity for Cr(VI) ions at the solid-liquid interface. This confirms the increasing randomness at the solid solution interface during adsorption. With increasing temperature, a slight change in the negative values of ΔG suggests that the adsorption process is less advantageous at high temperatures and preferable at low temperatures. These findings agree with thermodynamic studies from similar investigations in the reviewed literature (Mennas et al., 2023; Munagapati et al., 2022).

3.6 Effect of the presence of salts/electrolytes

Process effluent commonly comprises monovalent, divalent, and trivalent salts. As a result, it was crucial to understand how well the CNCs/N6@Fe_3O_4−CT nanocomposite adsorbent performs in such salts before treating any actual industrial effluent. Herein, it was investigated
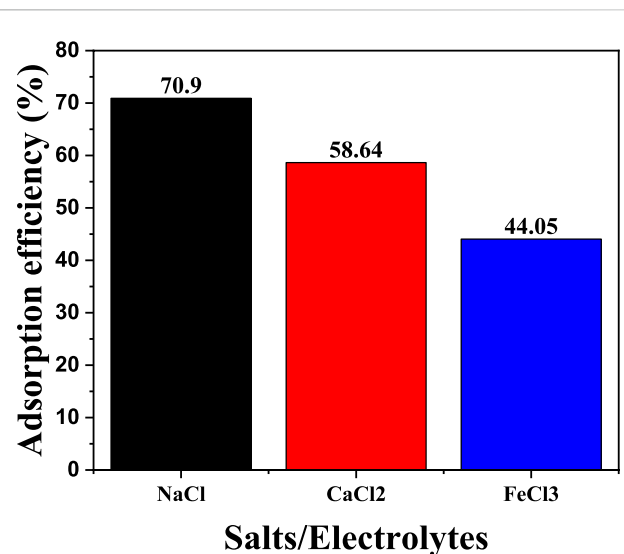
FIGURE 18
Effect of the presence of salts/electrolytes on adsorption of Cr^{6+}.

how well the CNCs/N6@Fe_3O_4−CT composite adsorbent performs in Cr(VI) adsorption in the presence of NaCl, $CaCl_2$, and $FeCl_3$ at 20 mg/L each. From the experimental data illustrated in Figure 18, the percentage removal of Cr(VI) decreased to 70.90%, 58.64% and 44.05% in the presence of NaCl, $CaCl_2$, and $FeCl_3$ salts, respectively. The findings suggest that the additional salt species could have interfered with the ability of the Cr(VI) ions to bind to the active sites on the CNCs/N6@ Fe_3O_4−CT surface, lowering its adsorption efficiency. Zhang et al. (2019) indicated that ionic strength also affects the equilibrium constant of the bulk liquid and adsorbent contact, which is crucial to the entire adsorption process (Zhang et al., 2019). The total metal ion's size, atomic radius, and molecular weight also significantly affect how

TABLE 4 Regeneration of CNCs/N6@Fe$_3$O$_4$–CT composite adsorbent using different eluents.

Cycles	Eluents					
	H2O		HCl		NaOH	
	% a	% D	% a	% D	% a	% D
1	91.23	16.02	91.23	88.67	91.23	96.36
2	8.75	2.33	53.21	71.62	77.79	84.12
3	1.34	0.224	33.22	28.35	56.28	69.76
4	–	–	18.56	11.12	44.32	33.25

[a]%A = percentage adsorption, %D = percentage desorption.

nanocomposite adsorbent adsorbs (Zhang et al., 2019). The impact of divalent and trivalent ions on transition metals is more significant than that of monovalent ions because Fe^{3+} contains more electrons in the outer orbit than earth metals, forming a surface complex with the adsorbent surface than Ca^{2+} and Na (Liu et al., 2016).

3.7 CNCs/N6@Fe$_3$O$_4$–CT adsorbent regeneration

The percentage desorption and adsorption efficiency of Cr(VI) were evaluated and presented in Table 4. From the experimental findings, water recorded the lowest desorption capacity, less than 10% in the first cycle. HCl and NaOH eluates produced more than 50% of their desorption capacities after two cycles before starting to drop. However, NaOH was identified to be more effective due to its excellent desorption efficiency, recording the highest among the three chosen desorption eluents. Studies show that when OH$^-$ions from basic solutions are present, they create chromate ions (CrO$_4^{2-}$), which are subsequently released into the solution when OH$^-$ions take their place on the adsorbent surface (Herath et al., 2021; Liao et al., 2022). Furthermore, the decline in the re-usability of the adsorbent was assumed to be a result of permanent or semi-permanent complex development (Equation 7), which makes desorption difficult. Given that, the prepared CNCs/N6@Fe$_3$O$_4$–CT nanocomposite adsorbent can be utilized for more than two cycles, and is made of low-cost materials (waste-based), and efficient synthesis procedure has the potential for optimization and application in domestic and industrial wastewater treatment.

4 Conclusion

The effectiveness of prepared CNCs/N6@Fe$_3$O$_4$–CT nanocomposite adsorbent in removing Cr(VI) metal ions is reported in this work. BET results showed that the nanocomposite material presents excellent porosity with a large surface area. FTIR spectra revealed the incorporation of functional groups from CNCs, N6 Fe$_3$O$_4$ and CT. The adsorption experiments showed that the adsorbent presented good sorption efficiencies at pH 2. An increased operating temperature minimally impacted the adsorption process, while the presence of ionic salts/electrolytes decreased the percentage removal for hexavalent chromium. NaOH was the best eluate due to its excellent desorption efficiency. The experimental data fitted well with the pseudo-second-order kinetic model. Furthermore, the isotherm models established that the Langmuir monolayer isotherm effectively predicted the adsorption process, which was confirmed by the R$_L$ values (0< R$_L$ <1). The order of isotherm model fitting was Langmuir > Freudlich > D–R > Temkin. The Gibbs free energy showed that the adsorption was favourable and spontaneous and that exothermic processes governed the adsorption process. Chemical adsorption dominated the process, with ion exchanges and the occurrence of chemical interactions. Given that the prepared CNCs/N6@Fe$_3$O$_4$–CT nanocomposite adsorbent was utilized for more than two cycles, this polymeric ferromagnetic nanocomposite adsorbent from low-cost materials (waste-based), biodegradable and efficient synthesis procedure has the potential for optimization and employed in industrial and domestic wastewater treatment.

Data availability statement

The raw data supporting the conclusions of this article will be made available by the authors, without undue reservation.

Author contributions

ES: Conceptualization, Formal Analysis, Methodology, Project administration, Writing–original draft, Writing–review and editing. HR: Conceptualization, Data curation, Resources, Supervision, Writing–review and editing. RM: Data curation, Software, Validation, Writing–review and editing. MB: Data curation, Software, Validation, Visualization, Writing–review and editing. TS: Conceptualization, Data curation, Resources, Supervision, Validation, Writing–review and editing. SK: Conceptualization, Methodology, Resources, Supervision, Validation, Visualization, Writing–review and editing. WM: Supervision, Conceptualization, Methodology, Validation, Writing–review and editing.

Conflict of interest

The authors declare that the research was conducted in the absence of any commercial or financial relationships that could be construed as a potential conflict of interest.

Publisher's note

All claims expressed in this article are solely those of the authors and do not necessarily represent those of their affiliated organizations, or those of the publisher, the editors and the reviewers. Any product that may be evaluated in this article, or claim that may be made by its manufacturer, is not guaranteed or endorsed by the publisher.

References

Abate, G. Y., Alene, A. N., Habte, A. T., and Getahun, D. M. (2020). Adsorptive removal of malachite green dye from aqueous solution onto activated carbon of *Catha edulis* stem as a low cost bio-adsorbent. *Environ. Syst. Res.* 9 (1), 29. doi:10.1186/s40068-020-00191-4

Adewumi, O. D., Olalekan, A., Dada, A., and Langmuir, A. O. (2012). Freundlich, Temkin and dubinin–radushkevich isotherms studies of equilibrium sorption of Zn 2+ unto phosphoric acid modified rice husk. *J. Appl. Chem.* 3, 38–45. doi:10.9790/5736-0313845

Al-Harby, N. F., Albahly, E. F., and Mohamed, N. A. (2021). Kinetics, isotherm and thermodynamic studies for efficient adsorption of Congo Red dye from aqueous solution onto novel cyanoguanidine-modified chitosan adsorbent. *Polymers* 13 (24), 4446. doi:10.3390/polym13244446

Ali Khan Rao, R., Rehman, F., and Kashifuddin, M. (2012). Removal of Cr(VI) from electroplating wastewater using fruit peel of Leech (*Litchi chinensis*). *Desalination Water Treat.* 49 (1–3), 136–146. doi:10.1080/19443994.2012.708211

Altun, T., and Ecevit, H. (2020). Cr (VI) removal using Fe2O3-chitosan-cherry kernel shell pyrolytic charcoal composite beads. *Environ. Eng. Res.* 25, 426–438. doi:10.4491/eer.2019.112

Ayoade, A., Adeyemi, A., Oyedeji, A., Adetoro, R., and Aderibigbe, F. (2020). Nanostructured and surface functionalized corncob as unique adsorbents for anionic dye remediation. *SN Appl. Sci.* 2, 301. doi:10.1007/s42452-020-2109-5

Babaei-Ghazvini, A., Vafakish, B., Patel, R., Falua, K. J., Dunlop, M. J., and Acharya, B. (2023). Cellulose nanocrystals in the development of biodegradable materials: a review on CNC resources, modification, and their hybridization. *Int. J. Biol. Macromol.* 258, 128834. doi:10.1016/j.ijbiomac.2023.128834

Banza, M., and Rutto, H. (2022). Extraction of cellulose nanocrystals from millet (Eleusine coracana) husk waste: optimization using Box Behnken design in response surface methodology (RSM). *Int. Nano Lett.* 12 (3), 257–272. doi:10.1007/s40089-022-00369-x

Biswas, S., Meikap, B. C., and Sen, T. K. (2019). Adsorptive removal of aqueous phase copper (Cu 2+) and nickel (Ni 2+) metal ions by synthesized biochar–biopolymeric hybrid adsorbents and process optimization by response surface methodology (RSM). Water. *Air, and Soil Pollut.* 230, 1–23. doi:10.1007/s11270-019-4258-y

Braver-Sewradj, S. P., Benthem, J, Staal, Y. C., Ezendam, J., Piersma, A. H., and Hessel, E. V. (2021). Occupational exposure to hexavalent chromium. Part II. Hazard assessment of carcinogenic effects. *Regul. Toxicol. Pharmacol.* 126, 105045. doi:10.1016/j.yrtph.2021.105045

Burtch, N. C., Jasuja, H., and Walton, K. S. (2014). Water stability and adsorption in metal–organic frameworks. *Chem. Rev.* 114 (20), 10575–10612. doi:10.1021/cr5002589

Chadha, U., Selvaraj, S. K., Thanu, S. V., Cholapadath, V., Abraham, A. M., Manoharan, M., et al. (2022). A review of the function of using carbon nanomaterials in membrane filtration for contaminant removal from wastewater. *Mater. Res. Express* 9 (1), 012003. doi:10.1088/2053-1591/ac48b8

Chaudhary, M., Singh, L., Rekha, P., Srivastava, V. C., and Mohanty, P. (2019). Adsorption of uranium from aqueous solution as well as seawater conditions by nitrogen-enriched nanoporous polytriazine. *Chem. Eng. J.* 378, 122236. doi:10.1016/j.cej.2019.122236

Claude, B. J., and Onyango, M. S. (2024). Continuous fixed-bed column adsorption of nickel (II) using recyclable three-dimensional cellulose nanocrystals-hydrogel: bed depth service time, Thomas, Adams–Bohart, and Yoon–Nelson modelling. *Can. J. Chem. Eng.* 102 (6), 2160–2171. doi:10.1002/cjce.25184

Cornell, R. M., and Schwertmann, U. (2003). *The iron oxides: structure, properties, reactions, occurrences, and uses*. Wiley-vch Weinheim. doi:10.1002/3527602097

Cristiano, E., Hu, Y.-J., Siegfried, M., Kaplan, D., and Nitsche, H. (2011). A comparison of point of zero charge measurement methodology. *Clays Clay Minerals* 59 (2), 107–115. doi:10.1346/CCMN.2011.0590201

Cruz-Lopes, L. P., Macena, M., Esteves, B., and Guiné, R. P. F. (2021). Ideal pH for the adsorption of metal ions Cr 6+, Ni 2+, Pb 2+ in aqueous solution with different adsorbent materials. *Open Agric.* 6 (1), 115–123. doi:10.1515/opag-2021-0225

Dhumal, R., and Sadgir, P. (2023). Bioadsorbents for the removal of salt ions from saline water: a comprehensive review. *J. Eng. Appl. Sci.* 70 (1), 80. doi:10.1186/s44147-023-00253-1

Dongre, R. S. (2021). Chromium and lead as soil pollutants: insights on toxicity profiles and their remediation. *J. Adv. Biotechnol. Bioeng.* 9, 1–16. doi:10.12970/2311-1755.2021.09.01

El-Kady, A. A., and Abdel-Wahhab, M. A. (2018). Occurrence of trace metals in foodstuffs and their health impact. *Trends food Sci. and Technol.* 75, 36–45. doi:10.1016/j.tifs.2018.03.001

Elwakeel, K. Z., Elgarahy, A. M., Khan, Z. A., Almughamisi, M. S., and Al-Bogami, A. S. (2020). Perspectives regarding metal/mineral-incorporating materials for water purification: with special focus on Cr (vi) removal. *Mater. Adv.* 1 (6), 1546–1574. doi:10.1039/D0MA00153H

Evans, S. K., Wesley, O. N., Koech, L., Nelana, S. M., and Rutto, H. L. (2022). Structural features of cellulose and cellulose nanocrystals via *in situ* incorporation of magnetic iron oxide nanoparticles: modification and characterization. *Coatings* 13 (1), 39. doi:10.3390/coatings13010039

Favela-Camacho, S. E., Samaniego-Benítez, E. J., Godínez-García, A., Avilés-Arellano, L. M., and Pérez-Robles, J. F. (2019). How to decrease the agglomeration of magnetite nanoparticles and increase their stability using surface properties. *Colloids Surfaces A Physicochem. Eng. Aspects* 574, 29–35. doi:10.1016/j.colsurfa.2019.04.016

Freundlich, H. M. F. (1906). Over the adsorption in solution. *J. Phys. Chem.* 57 (385471), 1100–1107. doi:10.12691/env-9-1-2

Guya, G. L. T. T. K. (2017). Impacts of tannery effluent on environments and human health. *J. Environ. earth Sci.* 7, 88–97.

Hassan, M., Liu, Y., Naidu, R., Du, J., Qi, F., Donne, S. W., et al. (2021). Mesoporous biopolymer architecture enhanced the adsorption and selectivity of aqueous heavy-metal ions. *ACS Omega* 6 (23), 15316–15331. doi:10.1021/acsomega.1c01642

Hassan, M., Liu, Y., Naidu, R., Parikh, S. J., Du, J., Qi, F., et al. (2020a). Influences of feedstock sources and pyrolysis temperature on the properties of biochar and functionality as adsorbents: a meta-analysis. *Sci. Total Environ.* 744, 140714. doi:10.1016/j.scitotenv.2020.140714

Hassan, M., Liu, Y., Naidu, R., Du, J., and Qi, F. (2020b). Adsorption of Perfluorooctane sulfonate (PFOS) onto metal oxides modified biochar. *Environ. Technol. and Innovation* 19, 100816. doi:10.1016/j.eti.2020.100816

Hassan, M., Naidu, R., Du, J., Liu, Y., and Qi, F. (2020c). Critical review of magnetic biosorbents: their preparation, application, and regeneration for wastewater treatment. *Sci. Total Environ.* 702, 134893. doi:10.1016/j.scitotenv.2019.134893

Herath, A., Layne, C. A., Perez, F., Hassan, E. B., Pittman Jr, C. U., and Mlsna, T. E. (2021). KOH-activated high surface area Douglas Fir biochar for adsorbing aqueous Cr (VI), Pb (II) and Cd (II). *Chemosphere* 269, 128409. doi:10.1016/j.chemosphere.2020.128409

Joseph, L., Jun, B.-M., Flora, J. R., Park, C. M., and Yoon, Y. (2019). Removal of heavy metals from water sources in the developing world using low-cost materials: a review. *Chemosphere* 229, 142–159. doi:10.1016/j.chemosphere.2019.04.198

Karak, N. (2009). *Fundamentals of polymers: raw materials to finish products*. New Delhi, India: PHI Learning Pvt. Ltd. doi:10.4236/ojpchem.2024.141004

Kerur, S. S., Bandekar, S., Hanagadakar, M. S., Nandi, S. S., Ratnamala, G. M., and Hegde, P. G. (2021). Removal of hexavalent Chromium-Industry treated water and Wastewater: a review. *Mater. Today Proc.* 42, 1112–1121. doi:10.1016/j.matpr.2020.12.492

Khan, F. S. A., Mubarak, N. M., Khalid, M., Walvekar, R., Abdullah, E. C., Mazari, S. A., et al. (2020). Magnetic nanoadsorbents' potential route for heavy metals removal—a review. *Environ. Sci. Pollut. Res.* 27, 24342–24356. doi:10.1007/s11356-020-08711-6

Kodama, R. H. (1999). Magnetic nanoparticles. *J. magnetism magnetic Mater.* 200 (1–3), 359–372. doi:10.1016/S0304-8853(99)00347-9

Kordbacheh, F., and Heidari, G. (2023). Water pollutants and approaches for their removal. *Mater. Chem. Horizons* 2 (2), 139–153. doi:10.22128/mch.2023.684.1039

Koul, B., Yadav, D., Singh, S., Kumar, M., and Song, M. (2022). Insights into the domestic wastewater treatment (DWWT) regimes: a review. *Water* 14 (21), 3542. doi:10.3390/w14213542

Lagergren, S. K. (1898). About the theory of so-called adsorption of soluble substances. Sven. *Vetenskapsakad. Handlingarl* 24, 1–39. doi:10.4236/aim.2024.146024

Langmuir, I. (1918). The adsorption of gases on plane surfaces of glass, mica and platinum. *J. Am. Chem. Soc.* 40 (9), 1361–1403. doi:10.1021/ja02242a004

Lesiak-Orłowska, B., Rangam, N., Jiricek, P., Gordeev, I, Toth, J., Kövér, L., et al. (2019). Surface study of Fe3O4 nanoparticles functionalized with biocompatible adsorbed molecules. *Front. Chem.* 7, 642. doi:10.3389/fchem.2019.00642

Li, T., Huang, X., Wang, Q., and Yang, G. (2020). Adsorption of metal ions at kaolinite surfaces: ion-specific effects, and impacts of charge source and hydroxide formation. *Appl. Clay Sci.* 194, 105706. doi:10.1016/j.clay.2020.105706

Liao, W., Zhou, X., Cai, N., Chen, Z., Yang, H., Zhang, S., et al. (2022). Simultaneous removal of cadmium, lead, chromate by biochar modified with layered double hydroxide with sulfide intercalation. *Bioresour. Technol.* 360, 127630. doi:10.1016/j.biortech.2022.127630

Liosis, C., Papadopoulou, A., Karvelas, E., Karakasidis, T. E., and Sarris, I. E. (2021). Heavy metal adsorption using magnetic nanoparticles for water purification: a critical review. *Materials* 14 (24), 7500. doi:10.3390/ma14247500

Liu, Z., Cao, M., Chen, Y., Fan, Y., Wang, D., Xu, H., et al. (2016). Interactions of divalent and trivalent metal counterions with anionic sulfonate gemini surfactant and induced aggregate transitions in aqueous solution. *J. Phys. Chem. B* 120 (17), 4102–4113. doi:10.1021/acs.jpcb.6b02897

Manzetti, S., and Van Der Spoel, D. (2015). Impact of sludge deposition on biodiversity. *Ecotoxicology* 24 (9), 1799–1814. doi:10.1007/s10646-015-1530-9

Mashile, G. P., Mpupa, A., Nqombolo, A., Dimpe, K. M., and Nomngongo, P. N. (2020). Recyclable magnetic waste tyre activated carbon-chitosan composite as an effective adsorbent rapid and simultaneous removal of methylparaben and propylparaben from aqueous solution and wastewater. *J. Water Process Eng.* 33, 101011. doi:10.1016/j.jwpe.2019.101011

McKinley, J. P., and Jenne, E. A. (1991). Experimental investigation and review of the "solids concentration" effect in adsorption studies. *Environ. Sci. Technol.* 25 (12), 2082–2087. doi:10.1021/es00024a015

Mennas, N., Lahreche, S., Chouli, F., Sabantina, L., and Benyoucef, A. (2023). Adsorption of methylene blue dye by cetyltrimethylammonium bromide intercalated polyaniline-functionalized montmorillonite clay nanocomposite: kinetics, isotherms, and mechanism study. *Polymers* 15 (17), 3518. doi:10.3390/polym15173518

Monshi, A., Foroughi, M. R., and Monshi, M. R. W. J. (2012). *Nano Sci. Eng.* 2, 154. doi:10.4236/wjnse.2012.23020

Mourya, V. K., Inamdara, N., and Ashutosh Tiwari, N. (2010). Carboxymethyl chitosan and its applications. *Adv. Mater. Lett.* 1 (1), 11–33. doi:10.5185/amlett.2010.3108

Munagapati, V. S., Wen, H.-Y., Gollakota, A. R., Wen, J.-C., Lin, K.-Y. A., Shu, C.-M., et al. (2022). Removal of sulfonated azo Reactive red 195 textile dye from liquid phase using surface-modified lychee (Litchi chinensis) peels with quaternary ammonium groups: adsorption performance, regeneration, and mechanism. *J. Mol. Liq.* 368, 120657. doi:10.1016/j.molliq.2022.120657

Munim, S., Muhammad, T. S, Saddique, M., Raza, Z., Raza, A., Majeed, M., et al. (2020). Fabrication of cellulose-mediated chitosan adsorbent beads and their surface chemical characterization. *Polym. Bull.* 77, 183–196. doi:10.1007/s00289-019-02711-4

Naja, G. M., and Volesky, B. (2017). "Toxicity and sources of Pb, Cd, Hg, Cr, As, and radionuclides in the environment," in *Handbook of advanced industrial and hazardous wastes management* (Boca Raton, FL: Crc Press), 855–903. doi:10.1201/9781420073195.ch2

Neto, J. O. M., Bellato, C. R., and Castro Silva, D. (2019). Iron oxide/carbon nanotubes/chitosan magnetic composite film for chromium species removal. *Chemosphere* 218, 391–401. doi:10.1016/j.chemosphere.2018.11.080

Nishat, A., Yusuf, M., Qadir, A., Ezaier, Y., Vambol, V., Khan, M. I., et al. (2023). Wastewater treatment: a short assessment on available techniques. *Alexandria Eng. J.* 76, 505–516. doi:10.1016/j.aej.2023.06.054

Nishu Kumar, S. (2023). Smart and innovative nanotechnology applications for water purification. *Hybrid. Adv.* 3, 100044. doi:10.1016/j.hybadv.2023.100044

Nthunya, L. N., Masheane, M. L., Malinga, S. P., Nxumalo, E. N., Mamba, B. B., and Mhlanga, S. D. (2017). Determination of toxic metals in drinking water sources in the chief albert luthuli local municipality in mpumalanga, South Africa. *Phys. Chem. Earth, Parts A/B/C* 100, 94–100. doi:10.1016/j.pce.2017.04.006

Ogunlalu, O., Oyekunle, I. P., Iwuozor, K. O., Aderibigbe, A. D., and Emenike, E. C. (2021). Trends in the mitigation of heavy metal ions from aqueous solutions using unmodified and chemically-modified agricultural waste adsorbents. *Curr. Res. Green Sustain. Chem.* 4, 100188. doi:10.1016/j.crgsc.2021.100188

Ouma, L., Pholosi, A., and Onani, M. (2022). Optimizing Cr(VI) adsorption parameters on magnetite (Fe$_3$O$_4$) and manganese doped magnetite (Mn$_x$Fe$_{(3-x)}$O$_4$) nanoparticles. *Phys. Sci. Rev.* 0 (0), 3885–3895. doi:10.1515/psr-2021-0149

Petrinic, I., Stergar, J., Bukšek, H., Drofenik, M., Gyergyek, S., Hélix-Nielsen, C., et al. (2021). Superparamagnetic fe3o4@ ca nanoparticles and their potential as draw solution agents in forward osmosis. *Nanomaterials* 11 (11), 2965. doi:10.3390/nano11112965

Pfeifer, A., and Skerget, M. (2020). A review: a comparison of different adsorbents for removal of Cr (VI), Cd (II) and Ni (II). *Turkish J. Chem.* 44 (4), 859–883. doi:10.3906/kim-2002-21

Pholosi, A., Naidoo, E. B., and Ofomaja, A. E. (2020). Intraparticle diffusion of Cr(VI) through biomass and magnetite coated biomass: a comparative kinetic and diffusion study. *South Afr. J. Chem. Eng.* 32, 39–55. doi:10.1016/j.sajce.2020.01.005

Qasem, N. A., Mohammed, R. H., and Lawal, D. U. (2021). Removal of heavy metal ions from wastewater: a comprehensive and critical review. *Npj Clean. Water* 4 (1), 36. doi:10.1038/s41545-021-00127-0

Rani, S., Sharma, S., Bansal, M., Garg, R., and Garg, R. (2022). Enhanced Zn (II) adsorption by chemically modified sawdust based biosorbents. *Environ. Sci. Pollut. Res.* 30, 99046–99061. doi:10.1007/s11356-022-22963-4

Rao, R. A. K., Ikram, S., and Uddin, M. K. (2015). Removal of Cr(VI) from aqueous solution on seeds of *Artimisia absinthium* (novel plant material). *Desalination Water Treat.* 54 (12), 3358–3371. doi:10.1080/19443994.2014.908147

Rápó, E., and Tonk, S. (2021). Factors affecting synthetic dye adsorption; desorption studies: a review of results from the last five years (2017–2021). *Molecules* 26 (17), 5419. doi:10.3390/molecules26175419

Rodríguez, M., Vázquez-Vélez, E., Martinez, H., and Torres, A. (2021). Superficial surface treatment using atmospheric plasma on recycled Nylon 6, 6. *J. Nucl. Phys. Material Sci. Radiat. Appl.* 8 (2), 191–196. doi:10.15415/jnp.2021.82025

Rudi, N. N., Muhamad, M. S., Te Chuan, L., Alipal, J., Omar, S., Hamidon, N., et al. (2020). Evolution of adsorption process for manganese removal in water via agricultural waste adsorbents. *Heliyon* 6 (9), e05049. doi:10.1016/j.heliyon.2020.e05049

Sadegh, H., Ali, G. A., Makhlouf, A. S. H., Chong, K. F., Alharbi, N. S., Agarwal, S., et al. (2018). MWCNTs-Fe3O4 nanocomposite for Hg (II) high adsorption efficiency. *J. Mol. Liq.* 258, 345–353. doi:10.1016/j.molliq.2018.03.012

Safitri, I., Wibowo, Y. G., and Rosarina, D. (2021). in *In Synthesis and characterization of magnetite (Fe3O4) nanoparticles from iron sand in Batanghari Beach* (IOP Publishing). doi:10.1088/1757-899X/1011/1/012020

Saha, P., and Chowdhury, S. (2011). Insight into adsorption thermodynamics. *Thermodynamics* 16, 349–364. doi:10.5772/13474

Salehi, M., Sharafoddinzadeh, D., Mokhtari, F., Esfandarani, M. S., and Karami, S. (2021). Electrospun nanofibers for efficient adsorption of heavy metals from water and wastewater. *Clean. Technol. Recycl.* 1, 1–33. doi:10.3934/ctr.2021001

Saravanan, A., Kumar, P. S., Jeevanantham, S., Karishma, S., Tajsabreen, B., Yaashikaa, P. R., et al. (2021). Effective water/wastewater treatment methodologies for toxic pollutants removal: processes and applications towards sustainable development. *Chemosphere* 280, 130595. doi:10.1016/j.chemosphere.2021.130595

Shakiba, M., Rezvani Ghomi, E., Khosravi, F., Jouybar, S., Bigham, A., Zare, M., et al. (2021). Nylon—a material introduction and overview for biomedical applications. *Polym. Adv. Techs* 32 (9), 3368–3383. doi:10.1002/pat.5372

Sharififard, H., and Rezvanpanah, E. (2021). Ultrasonic-assisted synthesis of SiO2 nanoparticles and SiO2/chitosan/Fe nanocomposite and their application for vanadium adsorption from aqueous solution. *Environ. Sci. Pollut. Res.* 28 (9), 11586–11597. doi:10.1007/s11356-020-11346-2

Sheth, Y., Dharaskar, S., Khalid, M., and Sonawane, S. (2021). An environment friendly approach for heavy metal removal from industrial wastewater using chitosan based biosorbent: a review. *Sustain. Energy Technol. Assessments* 43, 100951. doi:10.1016/j.seta.2020.100951

Singh, J., and Mishra, V. (2021). Simultaneous removal of Cu $^{2+}$, Ni $^{2+}$ and Zn $^{2+}$ ions using leftover *Azadirachta indica* twig ash. *Bioremediation J.* 25 (1), 48–71. doi:10.1080/10889868.2020.1843394

Singh, J., and Mishra, V. (2022). Development of sustainable and ecofriendly metal ion scavenger for adsorbing Cu2+, Ni2+ and Zn2+ ions from the aqueous phase. *Sep. Sci. Technol.* 57 (3), 354–371. doi:10.1080/01496395.2021.1913421

Smith, B. C. (2018). *Infrared spectral interpretation: a systematic approach.* Boca Raton, FL: CRC Press. doi:10.1201/9780203750841

Subedi, N., Lähde, A., Abu-Danso, E., Iqbal, J., and Bhatnagar, A. (2019). A comparative study of magnetic chitosan (Chi@ Fe3O4) and graphene oxide modified magnetic chitosan (Chi@ Fe3O4GO) nanocomposites for efficient removal of Cr (VI) from water. *Int. J. Biol. Macromol.* 137, 948–959. doi:10.1016/j.ijbiomac.2019.06.151

Suter, E., Rutto, H., Seodigeng, T., Kiambi, L., and Omwoyo, W. (2024a). Bagasse-based cellulose nanocrystal–magnetic iron oxide nanocomposite for removal of chromium (VI) from aqua media. *Eng. Proc.* 67 (1), 5. doi:10.3390/engproc2024067005

Suter, E. K., Rutto, H. L., Seodigeng, T. S., Kiambi, S. L., and Omwoyo, W. N. (2023a). Recycled pulp and paper sludge, potential source of cellulose: feasibility assessment and characterization. *J. Environ. Sci. Health, Part A* 58 (14), 1061–1071. doi:10.1080/10934529.2024.2309857

Suter, E. K., Rutto, H. L., Seodigeng, T. S., Kiambi, S. L., and Omwoyo, W. N. (2024b). Green isolation of cellulosic materials from recycled pulp and paper sludge: a Box-Behnken design optimization. *J. Environ. Sci. Health, Part A* 59, 64–75. doi:10.1080/10934529.2024.2331942

Suter, E. K., Rutto, H. L., Wesley, O. N., and Banza, M. (2023b). Stabilized bare superparamagnetic iron oxide nanoparticles: synthesis and characterization. *J. Nano Res.* 80, 81–96. doi:10.4028/p-f1ygDS

Temkin, M. I. (1941). Adsorption equilibrium and the kinetics of processes on nonhomogeneous surfaces and in the interaction between adsorbed molecules. *Zh. Fiz. Chim.* 15, 296–332.

Tlou, S., Suter, E., Alfred, M., Rutto, H., and Omwoyo, W. (2023). *In situ* capping of silver nanoparticles with cellulosic matrices from wheat straws in enhancing their antimicrobial activity: synthesis and characterization. *J. Environ. Sci. Health, Part A* 58 (11), 903–913. doi:10.1080/10934529.2023.2260295

Ugbea, F. A., Ikudayisi-Ugbeb, V. A., and Yakubuc, M. O. (2020). Adsorptive removal of Cd2+, Cr 3+ and Cr 6+ using natural and synthetic goethite particles: kinetics study. *J. New Technol. Mat.* 10 (02), 29–37. doi:10.12816/0058533

Unceta, N., Séby, F., Malherbe, J., and Donard, O. F. X. (2010). Chromium speciation in solid matrices and regulation: a review. *Anal. Bioanal. Chem.* 397 (3), 1097–1111. doi:10.1007/s00216-009-3417-1

Vaiopoulou, E., and Gikas, P. (2020). Regulations for chromium emissions to the aquatic environment in Europe and elsewhere. *Chemosphere* 254, 126876. doi:10.1016/j.chemosphere.2020.126876

Valentin, R., Bonelli, B., Garrone, E., Di Renzo, F., and Quignard, F. (2007). Accessibility of the functional groups of chitosan aerogel probed by FT-IR-monitored deuteration. *Biomacromolecules* 8 (11), 3646–3650. doi:10.1021/bm070391a

Varsha, M., Kumar, P. S., and Rathi, B. S. (2022). A review on recent trends in the removal of emerging contaminants from aquatic environment using low-cost adsorbents. *Chemosphere* 287, 132270. doi:10.1016/j.chemosphere.2021.132270

Wang, J., and Guo, X. (2023). Adsorption kinetics and isotherm models of heavy metals by various adsorbents: an overview. *Crit. Rev. Environ. Sci. Technol.* 53, 1837–1865. doi:10.1080/10643389.2023.2221157

Weber, W. J., and Morris, J. C. (1963). Kinetics of adsorption on carbon from solution. *J. Sanit. Engrg. Div.* 89 (2), 31–59. doi:10.1061/jsedai.0000430

Wise Jr, J. P., Young, J. L., Cai, J., and Cai, L. (2022). Current understanding of hexavalent chromium [Cr (VI)] neurotoxicity and new perspectives. *Environ. Int.* 158, 106877. doi:10.1016/j.envint.2021.106877

Xia, S., Song, Z., Jeyakumar, P., Bolan, N., and Wang, H. (2020). Characteristics and applications of biochar for remediating Cr(VI)-contaminated soils and wastewater. *Environ. Geochem Health* 42 (6), 1543–1567. doi:10.1007/s10653-019-00445-w

Xu, J., Ju, C., Sheng, J., Wang, F., Zhang, Q., Sun, G., et al. (2013). Synthesis and characterization of magnetic nanoparticles and its application in lipase immobilization. *Bull. Korean Chem. Soc.* 34 (8), 2408–2412. doi:10.5012/bkcs.2013.34.8.2408

Zhang, B., Hu, R., Sun, D., Wu, T., and Li, Y. (2018). Fabrication of chitosan/magnetite-graphene oxide composites as a novel bioadsorbent for adsorption and detoxification of Cr (VI) from aqueous solution. *Sci. Rep.* 8 (1), 15397. doi:10.1038/s41598-018-33925-7

Zhang, Y., Zhu, C., Liu, F., Yuan, Y., Wu, H., and Li, A. (2019). Effects of ionic strength on removal of toxic pollutants from aqueous media with multifarious adsorbents: a review. *Sci. Total Environ.* 646, 265–279. doi:10.1016/j.scitotenv.2018.07.279